Macedonian Journal of Chemistry and Chemical Engineering, Vol. **43**, No. 1, pp. 1–28 (2024)

MJCCA9 – 892

ISSN 1857-5552
e-ISSN 1857-5625

Received: March 27, 2024
Accepted: March 28, 2024

DOI: 10.20450/mjcce.2024.2858
Review

CROSSROADS OF VIBRATIONAL (INFRARED AND RAMAN) SPECTROSCOPY AND X-RAY POWDER DIFFRACTION IN IDENTIFICATION AND CHARACTERIZATION OF SOME MINERALS – ADVANTAGES AND LIMITATIONS. A REVIEW[1]

Petre Makreski[1,*], Ljupčo Pejov[1,2,3], Gligor Jovanovski[4,*]

[1]*Institute of Chemistry, Faculty of Natural Sciences and Mathematics, Ss. Cyril and Methodius University in Skopje, North Macedonia*
[2]*Department of Chemistry, Bioscience and Environmental Engineering, Faculty of Science and Technology, University of Stavanger, Norway*
[3]*The Polytechnic School, Ira A. Fulton Schools of Engineering, Arizona State University, AZ, USA*
[4]*Research Center for Environment and Materials, Macedonian Academy of Sciences and Arts, North Macedonia*

petremak@pmf.ukim.mk (PM); gligor@pmf.ukim.mk (GJ)

Many analytical methods have been successfully employed for the study of minerals, in particular, vibrational infrared (FTIR) and Raman spectroscopies and X-ray powder diffraction (XRPD). The advantages of the vibrational spectroscopic techniques for identifying and characterizing minerals include: rapid and versatile use; qualitative and quantitative chemical signatures; distinctive chemical fingerprint of a material; indirect determination of the crystal features (polymorphism, isomorphism, coordination, degree of deformation of structural polyhedra); small sample quantity (area less than 1 μm^2 for Raman); wide coverage of 4,000 – 50 cm^{-1} region in a single scan; in situ and direct measurements without sample preparation; nondestructive use; etc. On the other hand, XRPD is a destructive technique that, depending on the method used and the density of the material, requires from a few micrograms up to around 5 grams of sample quantity for analysis. In spite of that, it is a rapid and powerful technique used in mineral studies with relatively straightforward interpretation of the results. During the last decade, portable X-ray powder diffractometers for the nondestructive analysis of art and archeological materials have been developed along with the portable and hand-held vibrational spectroscopy instrument. Here, some advantages and limitations in the process of the complementary use of FTIR and Raman vibrational spectroscopy and XRPD for identification and characterization of minerals are outlined.

Keywords: vibrational spectroscopy; X-ray powder diffraction; advantages; limitations; minerals

ВКРСТУВАЊЕ НА ВИБРАЦИСКАТА (ИНФРАЦРВЕНА И РАМАНСКА) СПЕКТРОСКОПИЈА И РЕНДГЕНСКАТА ДИФРАКЦИЈА ОД ПРАШОК ПРИ ИДЕНТИФИКАЦИЈА И КАРАКТЕРИЗАЦИЈА НА НЕКОИ МИНЕРАЛИ – ПРЕДНОСТИ И ОГРАНИЧЕНОСТИ. ПРЕГЛЕДЕН ТРУД

Многу техники успешно се користат за изучување на минералите. Меѓу нив особено се издвојуваат вибрациските инфрацрвена (FTIR) и раманска спектроскопија и рендгенската дифракција од прашок (XRPD). Предностите на вибрациско-спектроскопските техники за идентификација и карактеризација се состојат во: брза и многустрана употреба; квалитативно и квантитативно хемиско одредување; разликување на хемиската природа на материјалот преку неговиот спектар; посредно определување на карактеристиките на кристалот (полиморфизам, изоморфизам, координација, степен на деформација на структурниот полиедар); мало количество

[1] Dedicated on the occasion of the Golden Jubilee of the *Macedonian Journal of Chemistry and Chemical Engineering*

на примерок (за раманската спектроскопија и површина помала од 1 μm^2); широк опфат на спектрална област од 4000 – 50 cm^{-1} преку само еден скен; *in situ* и директно снимање без подготовка на примерокот; недеструктивност врз примерокот итн. Од друга страна, XRPD е деструктивна техника за која, во зависност од методата која се користи и од густината на примерокот, за анализа е потребно од неколку милиграми до околу 5 грама примерок. И покрај тоа, тоа е брза и моќна техника која често се користи при испитувања на минералите, а се одликува со релативно едноставна интерпретација на резултатите. Во последната декада сè повеќе се развиваат и се користат т.н. преносни XRPD инструменти за недеструктивна анализа на уметнички и археолошки материјали, секако во спрега со соодветните рачни инфрацрвени и раманси спектрометри. Во овој прегледен труд е даден осврт на некои предности и ограниченост при комплементарно користење на FTIR и раманска спектроскопија, како и на XRPD за идентификација и карактеризација на различни минерали.

Клучни зборови: вибрациска спектроскопија; рендгенска дифракција од прашок; предности; ограниченост; минерали

1. INTRODUCTION

X-ray powder diffraction[1–3] and vibrational (infrared and Raman) spectroscopy[4–9] are the most widely used techniques for studying minerals. These methods provide valuable information about either the crystal or molecular structure of minerals, but there are some distinct advantages and limitations that one of the techniques has over the other. In this author's review, we will explore and discuss these aspects throughout the analysis of a large number of various types of minerals – anhydrous, hydrous, silicate, non-silicate, etc.

One of the primary advantages of vibrational spectroscopy is that it can provide detailed information about the chemical composition and chemical bonding in a mineral.[10] Infrared (IR) and Raman spectroscopy measure the way that a mineral absorbs and emits radiation in the corresponding regions of the electromagnetic spectrum. The obtained spectra can be used to identify the functional groups and the type of chemical bonds present in the mineral. In contrast, X-ray powder diffraction only provides evidence about the crystal structure of the mineral, but not necessarily for the chemical composition and the functional groups.

Another advantage of vibrational spectroscopy is that it can be used to characterize minerals whose analysis using other techniques is difficult or impossible. For example, some minerals may be too small or occur in mineral conglomeration or association to be individually analyzed using X-ray powder diffraction. In addition, vibrational spectroscopic techniques can be used to study minerals in situ, or in their natural environment, which can provide important insight into their behavior and properties under real-forming conditions. This is not possible with powder diffraction, which requires the mineral to be in a powdered form.[3] In contrast, powder diffraction data collection can be a more time-consuming process and cannot provide an answer to the presence of amorphous phases, which can be determined in both IR or Raman spectra since their building units also give unique spectral bands, regardless of the fact that the structures are not periodically arranged in three dimensions.

On the other hand, one of the main advantages of powder diffraction over vibrational spectroscopy is that it can provide a complete crystal structure analysis.[11] This means that not only can the unit cell dimensions and space group be determined, but also the positions of all the atoms in the crystal can be located. In addition, powder diffraction also has the advantage of being able to simultaneously determine the presence of a wide range of minerals. This technique can be used to identify both common and rare minerals, and it can provide information about their crystal structure and composition, because the peaks in the diffraction patterns are narrower and less complex to interpret in comparison to the vibrational bands in the spectra. The positions of the X-ray powder diffraction maxima are constant (and easier to interpret), which is not always the case with the position of the vibrational bands in the Raman and infrared spectra arising from the functional group, as they might be shifted depending on their cation (metal, hydrogen) or anion (OH) arrangement.

There are cases of powder XRD dominance over single-crystal XRD. Namely, reliable results can be obtained using X-ray powder diffraction, which make it possible to obtain good resolution of reflections, determine reliable values of unit cell parameters (comparable to those obtained by single-crystal X-ray diffraction), and carry out credible identification of structurally similar minerals.[12] Another advantage is that powder XRD can be done a mixture and using Rietveld analysis determine composition whereas single-crystal XRD requires a single phase.

On the other hand, micro-Raman spectroscopy has some advantages over infrared spectroscopy. The former is a non-destructive technique, so the sample can be used for other studies or analyses, which is particularly important for gems and valuable specimens. This allows multiple techniques to be used on the same sample, which can provide a more complete picture of the analyzed mineral.[13]

In parallel to the above-mentioned experimental techniques, the present review also scrutinizes the relevance of state-of-the-art theoretical modeling techniques that have been used as a tool for more exact and more reliable interpretation of the experimental data. In many cases, even when quantitative agreement between theoretical and experimental data cannot be achieved, theory still predicts the right order of appearance of bands in the vibrational spectra of these complex solid-state systems and solely by inspecting the resemblance between the theoretical and experimental spectral patterns more detailed assignments can be provided.

2. MATERIALS AND METHODS

2.1. *Experimental*

The following samples were natural minerals collected mainly from deposits in N. Macedonia: almandine [$Fe_3Al_2(SiO_4)_3$] from Staro Bonče; beryl [$Be_3Al_2Si_6O_{18}$] from Čanište; hematite [Fe_2O_3] from Damjan and Ržanovo; rutile [TiO_2] from Veselčani; jarosite [$KFe_3(SO_4)_2(OH)_6$] from Bukovik; struvite [$MgNH_4PO_4{\cdot}H_2O$] from Crni Vrv; and stibnite [Sb_2S_3], realgar [α-AsS], pararealgar [AsS], parapierrotite [$TlSb_5S_8$], hörnesite [$Mg_3(AsO_4)_2{\cdot}8H_2O$] and picropharmacolite [$Ca_4Mg(AsO_3OH)_2(AsO_4)_2{\cdot}11H_2O$] from Allchar (Fig. 1). Other studied minerals were collected throughout the world: symplesite [$Fe_3(AsO_4)_2{\cdot}8H_2O$] from Laubach (Germany); pharmacolite [$Ca(AsO_3OH){\cdot}2H_2O$] from Saru Dornei (Romania); and vladimirite [$Ca_4(AsO_3OH)(AsO_4)_2{\cdot}4H_2O$] from White Caps Mine, Nevada (USA) (Fig. 1). The following samples were synthetic analogues to the minerals: pyrargyrite [Ag_3SbS_3], stibioellisite [Tl_3SbS_3], miargyrite [$AgSbS_2$] and weissbergite [$TlSbS_2$] and were prepared by solid-state reactions in sealed quartz tubes.[14,15] The natural samples were carefully separated from the ore sample under an optical microscope. All samples were powdered prior to taking vibrational spectroscopy and XRPD measurements.

The Perkin Elmer 2000 FTIR interferometer was employed for recording the room temperature (RT) and liquid nitrogen temperature (LNT) mid-IR spectra using the KBr pellet method (4000 – 400 cm^{-1}). The pellet was prepared by distributing 1 mg of the powdered sample into 250 mg KBr (for IR spectroscopy, Merck) and applying a pressure of 10 t/cm^2. A Graceby Specac P/N 21525 variable-temperature cell (Graceby Specac, Orpington, Kent, UK) with KBr windows was used for the LNT measurements. The resolution of the instrument was 4 cm^{-1} and each spectrum was averaged from 16 scans (accumulations). The far-IR spectra were recorded on the same instrument (650 – 50 cm^{-1}) using suspension mulls of the samples with Nujol between polyethylene plates. The number of scans was set to 512 and the resolution was 4 cm^{-1}.

A micro-Raman multichannel spectrometer, Horiba JobinYvon LabRam Infinity (f × 100) with either 532 nm Nd:YAG laser line or He:Ne laser (632.8 nm), was used for recording the spectra. Additionally, the almandine sample was recorded by other conventional (dispersive) and Fourier transform Raman instruments. In particular, Renishaw micro-Raman 1000 spectrometer using the 514 nm excitation line of an air-cooled argon ion laser (Melles Griot), as well as the Dilor Z24 triple dispersive monochromator with Coherent Innova 400 operating at 488 nm Ar laser line (4 scans, resolution 4 cm^{-1}) were used. A Bruker FT Raman model 106/S connected to FTIR interferometer Equinox 55 with 1064 nm line of Nd:YAG frequency laser was employed to collect the FT-Raman spectrum (1024 scans, resolution 4 cm^{-1}) of stibnite as well.

The X-ray powder diffraction patterns of the minerals were recorded on a Philips PW 3710 X-ray diffractometer from 8 to 120° 2θ (step size 0.01°, time per step 2.5 s). A X-ray generator with 50 kV and a current of 30 mA was employed as a source for Cu $K\alpha$ radiation. The mineral sample was powdered and manually positioned over a silicon sample plate. The diffractograms were analyzed by the Fullprof program, and the ICDD-PDF-2 database for phase identification and peak indexing was employed.

For the crystal structure solution of symplesite, a Stoe Stadi-P powder diffractometer was used [Mo $K\alpha_1$, radiation from primary Ge(111) Johannson-type monochromator and using a Mythen Dectris 1K detector]. The powdered sample was sealed in a borosilicate glass capillary (0.5 mm diameter Hilgenberg glass capillary No. 50), which was spun during the measurement for better data statistics. Diffraction data for the crystal structure solution were collected from 3° to 42° 2θ for a period of 24 h, with more detailed information given in Runčevski et al.[16]

Almandine [$Fe_3Al_2(SiO_4)_3$] from Staro Bonče

Beryl [$Be_3Al_2Si_6O_{18}$] from Čanište

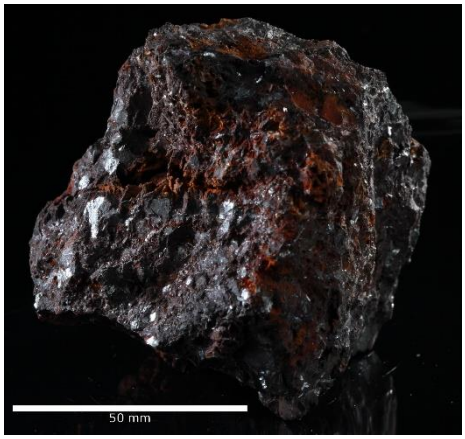

Hematite (Fe_2O_3) from Damjan

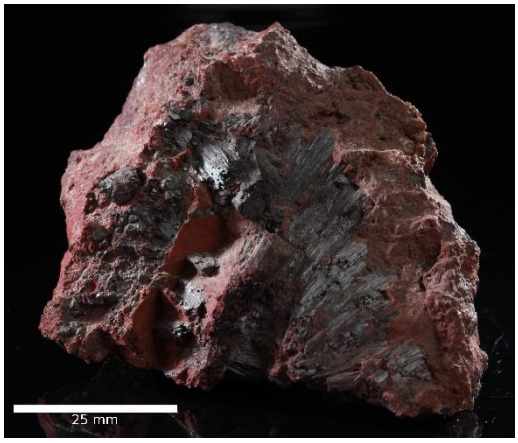

Hematite (Fe_2O_3) from Ržanovo

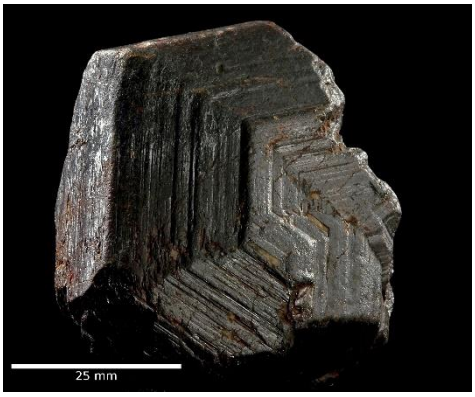

Rutile (TiO_2) from Veselčani

Stibnite (Sb_2S_3) from Allchar

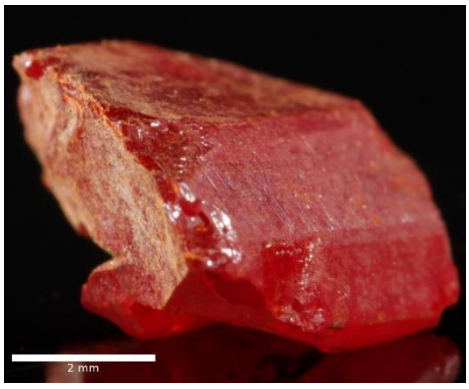

Realgar (α-AsS) from Allchar

Pararealgar (AsS) from Allchar

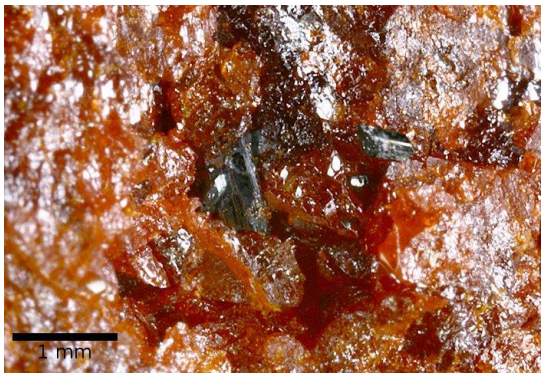

Parapierrotite ($TlSb_5S_8$) from Allchar

Pharmacolite [$Ca(AsO_3OH)\cdot 2H_2O$] from Saru Dornei, Romania

Hörnesite [$Mg_3(AsO_4)_2\cdot 8H_2O$] from Allchar

Vladimirite [$Ca_4(AsO_3OH)(AsO_4)_2\cdot 4H_2O$] from White Caps Mine, USA

Picropharmacolite [$Ca_4Mg(AsO_3OH)_2(AsO_4)_2\cdot 11H_2O$] from Allchar

Symplesite [$Fe_3(AsO_4)_2\cdot 8H_2O$] from Laubach, Germany

Struvite ($MgNH_4PO_4\cdot H_2O$) from Crni Vrv

Jarosite [$KFe_3(SO_4)_2(OH)_6$] from Bukovik

Fig. 1. The photographs of the studied minerals

2.2. *Theoretical techniques*

Appearance of a band in the vibrational spectrum of a given material indicates a transition with a certain energy difference between the vibrational levels, corresponding to the energy of the absorbed IR photon. However, the experimental data does not give any additional information about the studied system, e.g., the nature or origin of the involved levels. Therefore, performing theoretical calculations in order to provide support or even offer a thoroughly new understanding of the experimentally observed pattern has become a standard in contemporary science.

In a number of our previous studies, different theoretical approaches for the previously outlined purposes, based on the periodic density functional theory (DFT), have been implemented. The first one of these is the pseudopotential plane-wave (PSPW) density functional theory approach (PSPW DFT), while the second one is based on the representation of the one-particle wavefunctions (often called crystal orbitals) as linear combinations of Bloch functions. The Bloch functions are, on the other hand, expressed through atomic orbitals (i.e., local functions). The particular implementation of the PSPW DFT approach used is the one in the NWCHEM series of codes, while the second is the one in the CRYSTAL series of codes. The DFT implementation is based on the Kohn-Sham formalism, in which the energy of the system is written in the form of the Kohn-Sham functional:

$$E[\{\psi_i\}] = 2\sum_i \int \psi_i \left[-\frac{\hbar^2}{2m}\right] \nabla^2 \psi_i d^3\vec{r} + \int V_{\text{ion}}(\vec{r})\rho(\vec{r})d^3\vec{r} + \frac{e^2}{2}\int \frac{\rho(\vec{r})\rho(\vec{r}')}{|\vec{r}-\vec{r}'|} d^3\vec{r} d^3\vec{r}' + \tag{1}$$

where in equation (1), E_{ion} is the Coulomb energy of interionic interactions, $\{R\}$ denotes the momentary set of ionic (i.e., nuclear) positions, V_{ion} is the interaction potential between electrons and ions, and $E_{\text{xc}}[\rho(r)]$ is the exchange-correlation energy functional. The electron density is defined as:

(2)

Choosing the set of one-electron wavefunctions $\{\psi_i\}$ such that the Kohn-Sham functional is minimized, arrives at the Kohn-Sham equations:

(3)

In equation (3), ε_i are the energy eigenvalues of the Kohn-Sham Hamiltonian and V_{H} is the Hartree electronic potential. The single-particle orbitals, within the plane-wave expansion formalism, can be written in the following form:

$$\psi_{\alpha\vec{k}}(\vec{r}) = \exp\left(i\vec{k}\vec{r}\right)\sum_{\vec{G}} \tilde{\psi}_{\alpha\vec{k}}(\vec{G})\exp\left(i\vec{G}\vec{r}\right) \tag{4}$$

In equation (4), $\vec{k}$ is a vector within the first Brillouin zone; $\vec{G}$, on the other hand, denotes the set of reciprocal lattice vectors. The nonlocal pseudopotential term in the PSPW Kohn-Sham equations has the form:

$$v_a^{ps}(\vec{r},\vec{r}') = \sum_a v_a^{ps}\left(\vec{r}-\vec{R}_a, \vec{r}'-\vec{R}_a\right) \tag{5}$$

The complexity of electron-electron interactions in many-electron systems, within the DFT approach, is contained within the exchange-correlation potential $v^{xc}(\vec{r},\vec{r}')$. It can have two basic forms: local and nonlocal. The local variant is a simple, local multiplicative potential:

$$v^{xc}(\vec{r},\vec{r}') = v_{loc}^{xc}(\vec{r})\delta(\vec{r}-\vec{r}') \tag{6}$$

In a more realistic scenario involving the nonlocal effects, v^{xc} acts as an integral operator. In our previous studies based on local density approximation (LDA), a Vosko's functional[17] has been implemented to solve the Kohn-Sham (KS) equations in an iterative manner. The valence electrons' wavefunctions were represented by expansion in a plane-wave basis set, while to account for the interactions between the valence shell electrons and the nuclei and core electrons, the pseudopotential approach was used. In our previous studies, the norm-conserving Hamann pseudopotential[18] was used for As, O and H atoms, with the nonlocal part modified to a completely separable form, according to Refs.[19,20] and Troullier-Martins norm-conserving pseudopotentials[21] on Mg and Fe. A series of extensive test calculations has been done for each of the studied systems to arrive at the parameters that should be implemented for the actual productive calculations. Such tests have been done, e.g., by discretization along lattice vector directions in order to determine an appropriate grid of points which will be further used to allow suffi-

cient convergence. Our previous studies carried out the Ewald summation over several unit cells in each spatial direction to ensure appropriate convergence. Along with the Vosko's functional, a series of different systems were studied by numerous test calculations with other nonlocal exchange-correlation functionals, such as PBE96, PBESOL etc. The geometries of the used 3D periodic model systems were optimized with the Grassman LMB-FGS energy minimization scheme. Usually, two geometry optimization procedures were implemented. The first one allowed both the atomic positions within the unit cell as well as the unit cell parameters themselves to vary in the course of optimization. Conversely, in the second one, the unit cell parameters were kept fixed (at the experimentally determined values), while the atomic positions within the unit cell were allowed to vary during optimization. By carrying out numerous test calculations using both approaches, the conclusion was derived that the second procedure often led to much more reliable data and, at the same time, provided significantly better agreement with the experiment. Sequentially to geometry optimization, harmonic vibrational analysis was carried out based on analytic computation of the nuclear Hessian matrix using the first-derivative of the analytical gradients. To project out the translations and rotations of the nuclear Hessian, we have used the standard Eckart projection algorithm.

3. RESULTS AND DISCUSSION

This section outlines the advantages and limitations of XRPD and vibrational spectroscopy for identification purposes of the minerals studied. The examples are sorted out by pinpointing the superiority of some of the techniques over the other. Since they have their own advantages and disadvantages, it is recommended to use them as complementary rather than competitive techniques. Sometimes, however, it is necessary to use only one of the above-mentioned techniques. In addition, the usefulness of theoretical techniques to support and assist the empirical assignments of the spectral bands was also addressed. Theoretical studies are a valuable tool to initiate reassignments and substantial reconsideration of the factors leading to certain trends in the vibrational frequencies.

3.1. *XRPD dominance over vibrational (infrared) spectroscopy*

3.1.1. *Rutile*

The IR spectrum of rutile is extremely sensitive to size, shape and preparatory sample conditions.[4,22,23] The reason behind this is due to its high refraction index that causes spectral differences that are predominantly expressed in the IR rather than in the corresponding Raman spectrum.[4] Thus, the spectral manifestation varies in terms of broadening of the bands as well as in the shift of the band maxima (Fig. 2).[23–26] Therefore, the IR active modes give rise to four bands in the far IR spectrum of our analyzed rutile sample (Fig. 2g).[27] As presented in Table 1, the observed four IR bands in the spectrum of the studied rutile sample appear in the expected broadened spectral regions. In spite of that, the identification of the minerals with high refraction index, as in the case of the rutile sample, should be additionally proved by the use of more reliable methods.

T a b l e 1

Band assignment and frequencies (in cm^{-1}) in the IR spectra of rutile from Veselčani compared to corresponding literature data (data from Ref.[27])

Description	Our work (Veselčani)	Ocana & Serna[23], natural[b]	McDevitt & Baun[24], synthetic	Luxon & Summitt[25], natural[a]
– ν_3	334 m[c]	365 – 345	352 w	350
– ν_2	398 m	435 – 405	423 w	425
E_u^3 – ν_1	528 w	545 – 515	608 s	610
– ν_4	600 s	675 – 600	695 s	680

[a] The intensities are not given.
[b] The range for band appearance is given because six spectra are observed. Intensity varies.
[c] s – strong; m – medium; w – weak.

In our recent study of rutile vibrational dynamics, a combined molecular dynamics (MD) approach, in conjunction with the linear response theory-based analysis of the trajectories, was carried out to compute the temperature-perturbed infrared response of TiO_2 with the generalized two-

dimensional correlation analysis of the obtained spectra.[28] We have used the second-order self-consistent charge density functional tight binding (SCC-DFTB) approach for 3D periodic systems to carry out the MD simulations. The study demonstrated the usefulness of the approach and its potential to get further insights into the vibrational dynamics of periodic systems by combining statistical physics simulations with the generalized two-dimensional correlation spectroscopy (2D COS) analysis. By carrying out an in-depth analysis of the synchronous and asynchronous 2D spectra, a significant new insight into the anharmonic couplings between the modes in the studied system was provided. In addition, the sequential character of the temperature-induced changes in the vibrational force field was also rationalized.

T a b l e 2

The most intense maxima in the X-ray diagram of rutile from Veselčani compared to the literature data (data from Ref.[27])

	Our work		Berry & Thompson[29]	Berry[30,a]
hkl	***I/I*$_0$**	***d*$_{exp}$ (Å)**	***d*$_{exp}$ (Å)**	***d*$_{exp}$ (Å)**
110	100	3.21	3.24_{10}	3.25_x
101	32	2.46	2.49_5	2.49_5
200	8	2.23	$2.29_{1/2}$	
111	15	2.17	2.18_3	2.19_3
210	7	2.04	$2.05_{1/2}$	
211	33	1.68	1.687_7	1.69_6
220	9	1.62	1.621_3	1.62_2
002	6	1.47	1.473_1	1.46_1
130	6	1.45	1.451_1	
031	12	1.35	1.354_4	1.35_2
112	8	1.34	1.344_1	
321	5	1.18	1.169_1	
222	5	1.09	1.092_1	
141	5	1.04	$1.041_{1/2}$	

[a] Synthetic analogue.

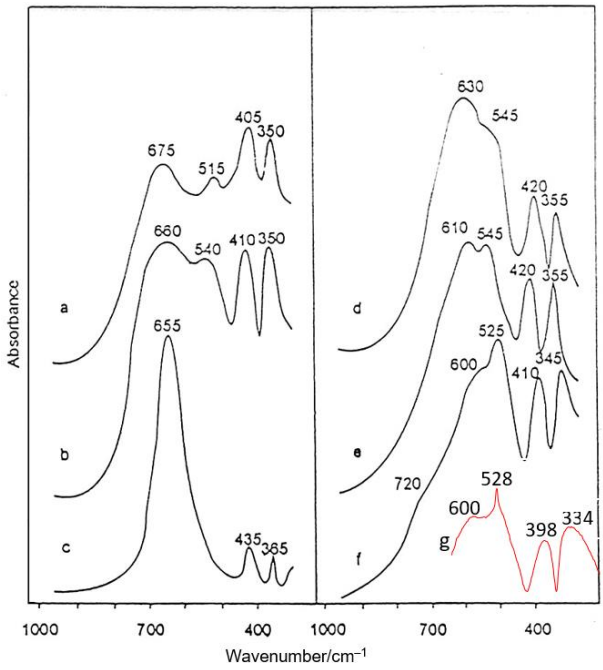

Fig. 2. The IR spectra (a-f) of various synthetic and commercial rutile samples[23] compared to the spectrum of rutile (g) from Veselčani

To avoid possible misidentification and misinterpretation of the nature of the rutile samples, a more reliable method is recommended. Therefore, the sample was analyzed by X-ray powder diffraction. Table 2 lists the characteristic peaks in the studied powder diagram[27] compared with the cor-

responding maxima in the diagrams of natural[29] and synthetic[30] rutile samples. The comparison shows that the results from the X-ray powder pattern of the studied rutile sample are practically identical with the diagrams of the natural rutile taken from the literature. The characterization of the studied mineral sample shows that XRPD is certainly a more reliable technique for identification of the studied rutile sample compared to FTIR spectroscopy.

3.1.2. *Hematite*

Two hematite samples were studied[27] in the far-infrared region (Fig. 3). Very pronounced spectral similarity strongly indicates that the investigated samples belong to the same mineral. The observed six bands in the spectra of the studied samples correspond, in general, to the number of the infrared bands (four to six) reported in the literature,[4,24,26,31] (Table 3) and are in agreement with the predictions based on the factor-group analysis.[6] The observed frequency shifts of the corresponding bands (Fig. 3, Table 3) in the studied spectra were explained as due to the influence of the particle shape and size.[26]

3

Band assignment and frequencies (in cm^{-1}) in the IR spectra of hematite samples from Damjan and Ržanovo compared to corresponding literature data (from Ref.[27])

Mode	Our work		Taylor *et al.*[31], natural	Farmer[4], natural[a]	McDevitt & Baun[24], synthetic	Serna *et al.*[26], synthetic[b]	
	Ržanovo						
E_u^1	641m[c]	643 m	625 sh	650 w	630 sh	–	–
E_u^2	453 s	446 s	465 s	440 s	470 s	480 s	468 s
E_u^3	315 s	307 s	335 s	–	335 s	345 s	325 s
E_u^4	233 w	233 w	–	229 w	229 w	235 w	–
A_{2u}^1	528 s	526 s	545 s	525 s	540 s	560 s	560 s
A_{2u}^2	397 w	397 w	370 sh	400 sh	380 w	370 sh	370 sh

[a] The band frequencies are approximate because numeric data are not given.
[b] First column – lath-shaped microcrystals; second column – very irregularly shaped particles.
[c] s – strong; m – medium; w – weak; sh – shoulder.

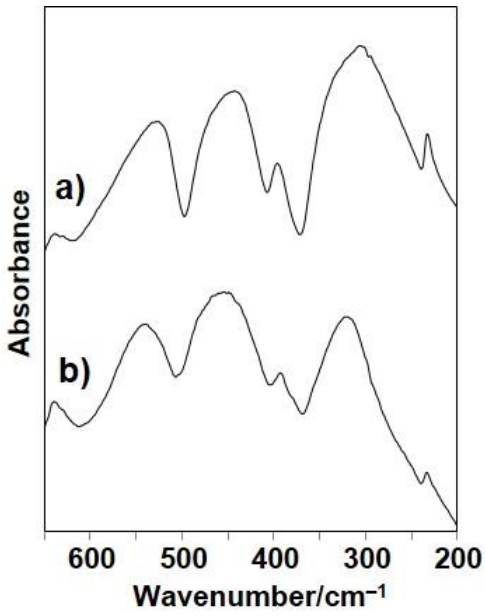

Fig. 3. The far-IR spectra of hematite from Damjan (a) and Ržanovo (b)

In order to confirm the insights obtained by infrared spectroscopy, the X-ray diagrams of the studied samples were obtained.[27] Several peaks in their X-ray patterns[32] (not shown here) were not typical for hematite and were attributed to the presence of talc and orthochrysotile impurities in the Ržanovo sample as well as to the quartz impurities in the Damjan sample (Table 4).

It is again evident that, compared to the applied FTIR method, the XRPD is a more reliable technique for detecting the presence of various types of impurities in the studied two hematite samples. This scenario comes into mind particularly for the oxide and sulfide samples whose absorption bands rest in the far-IR region where the remaining oxygen-containing minerals (carbonates, sulfates, phosphates, arsenates, vanadates, arsenates, silicates, etc.), do not show pronounced peaks and can hardly be detected when present as an impurity in oxides, sulfides and/or sulfosalts.

4

The impurity maxima in the X-ray diagram of hematite

from Ržanovo and Damjan compared to the literature data (adapted from Ref.[27])

Our work (Ržanovo)		Our work (Damjan)		Impurities (Assignment from Berry & Thompson[29])
I/I_0	d_{exp} (Å)	I/I_0	I/I_0	d_{exp} (Å)
12	9.03			9.35_x – Talc
15	6.88			7.10_x – Orthochrysotile
8	4.67			4.59_6 – Talc
10	3.51			3.55_7 – Orthochrysotile
		14	3.28	3.34_x – Quartz
20	3.05			3.12_4 – Talc
		9	2.27	2.28_4 – Quartz
6	2.27			2.33_8 – Orthochrysotile

3.2. *Vibrational spectroscopy dominance over XRPD*

3.2.1. *Beryl*

While beryl [$Be_3Al_2Si_6O_{18}$] is generally considered a nominally anhydrous mineral, the infrared spectrum obtained at room temperature for the beryl sample from Čanište reveals bands indicating the presence of water molecules (H_2O) and hydroxyl groups (OH). The spectrum indicates two distinct bands at 3592 cm^{-1} (B-notation) and 3660 cm^{-1} (C-notation), as shown in Fig. 4a. In contrast, the infrared spectrum obtained at liquid nitrogen temperature (LNT) exhibits an additional weak band at 3697 cm^{-1} (A-notation), as shown in Fig. 4b.[33] This spectral deviation strongly suggests the presence of a particular type of H_2O molecules predominantly occupying channels along the *c*-axis in the beryl structure.[34,35] Specifically, the bands observed in the 3690 – 3699 cm^{-1} and 3629 – 3650 cm^{-1} regions (refer to Table 4[33]) represent type I H_2O molecules, which are arranged with their symmetry axis perpendicular to the channel axis, a characteristic feature of alkali-free beryls. These bands are almost absent in our room temperature spectrum. Conversely, the bands corresponding to the stretching vibrations of type II H_2O molecules (associated with alkali-bearing beryls) appear in the 3660 – 3674 cm^{-1} and 3590 – 3596 cm^{-1} region, which are distinctive features of the studied beryl specimen. Furthermore, the bending vibration of H_2O (1623 cm^{-1}, inset in Fig. 4) provides additional evidence for the presence of type II H_2O molecules, as its wavenumber is approximately 20 cm^{-1} higher than the corresponding band for type I H_2O molecules (the latter band is absent in our IR spectrum). The studied beryl does not contain a third type of H_2O with the same *C*2 symmetry axis orientation as type I water,[34] nor does it contain CO_2 molecules, as indicated by the absence of bands associated with their infrared active modes (refer to Table 4[33]).

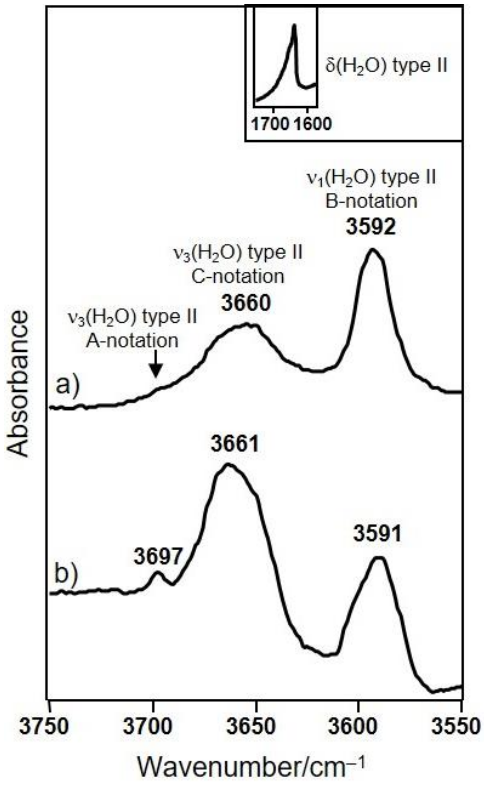

Fig. 4. FTIR spectrum of beryl from Čanište recorded at RT (a) and at LNT (b) in the stretching H_2O region. Inset: The bending H_2O region.

The Raman spectrum of beryl in the stretching region of H_2O (Fig. 5a) aligns with the expectations based on the corresponding IR spectrum.[33] Specifically, the prominent band at 3596 cm^{-1} can be confidently attributed to the ν_1 mode of type II water molecules, while the band with very weak intensity at 3663 cm^{-1} may be related to the corresponding ν_3 vibration. The band resulting from the deformations of H_2O molecules is fingerprinted as a weak band and appears at 1610 cm^{-1} (Fig. 5b). No bands related to type I water molecules are detected in either the stretching or bending regions, providing further indirect confirmation of their

absence in the crystal structure of the analyzed beryl specimen.

Here it should be pointed out that X-ray powder diffraction is not a suitable technique for detecting the presence of water molecules in the studied beryl sample.

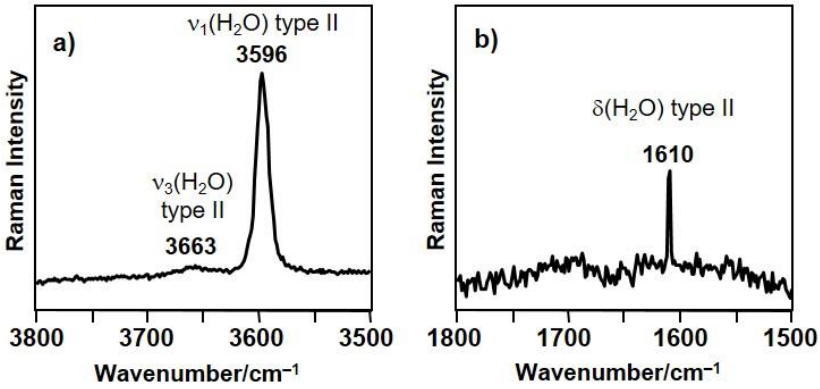

Fig. 5. Raman spectrum of beryl from Čanište in the stretching H_2O region (a) and bending H_2O region (b)

3.3. *Infrared spectroscopy dominance over Raman spectroscopy*

3

.

5

Symplesite and hörnesite

Despite the intricate structural composition of symplesite, $[Fe_3(AsO_4)_2{\cdot}8H_2O]$, and hörnesite $[Mg_3(AsO_4)_2{\cdot}8H_2O]$, the spectral characteristics of both minerals can be systematically and relatively easily analyzed by dividing the overall spectrum into distinct regions associated with vibrations of the crystalline water molecules and the molecular anions (AsO_4^{3-}), connected by the corresponding cations.[36] The objective here is to emphasize the ability to identify and correlate the infrared and Raman bands originating from water vibrations.

The presented infrared spectrum of symplesite in Figure 6a exhibits a striking similarity to previously reported data.[4,37] Notably, due to the complex hydrogen bonding network, a broad band resulting from H_2O stretching vibrations appears in the symplesite IR spectrum within the 3500 – 2800 cm^{-1} range, with two peaks observed at 3377 cm^{-1} and 3000 cm^{-1} (Fig. 6a). Additionally, the bending mode of water molecules is represented by a peak at 1630 cm^{-1}, closely resembling literature findings.[4,37]

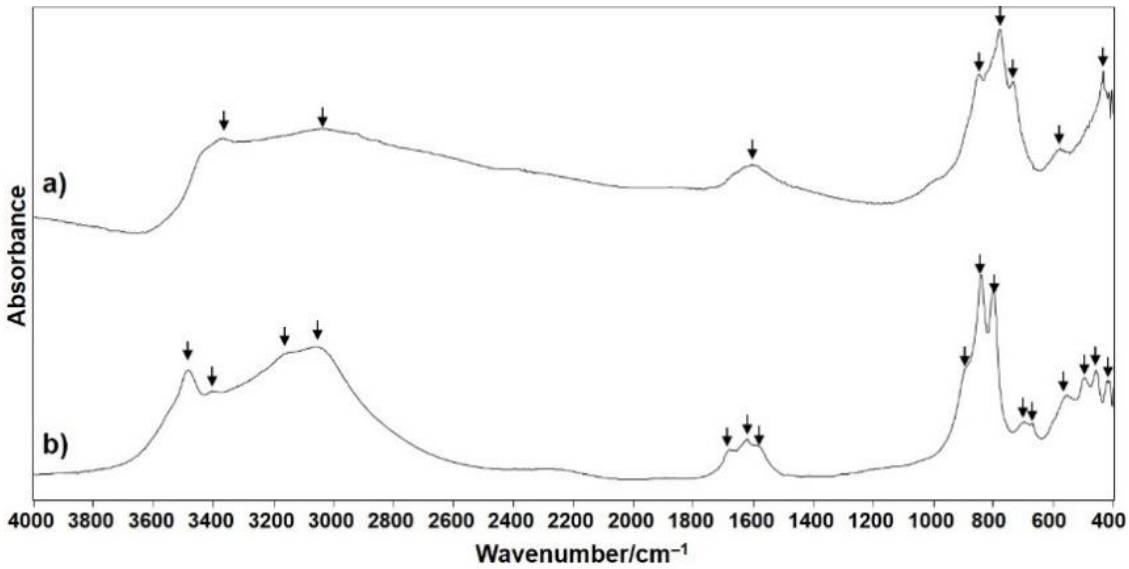

Fig. 6. Experimental IR spectra of symplesite (a) and hörnesite (b). The wavenumbers of the prominent peaks are marked by arrows.

In both symplesite (with Fe)[16] and hörnesite (with Mg)[38] structures, the octahedral arrangement of arsenate and water oxygen atoms around the metal (M) atom forms a repeating unit,

$M_2O_6(H_2O)_4$, which is connected to two similar neighboring units as well as four individual octahedral species of the form $MO_2(H_2O)_4$. Through such linking, which extends infinitely in an ideal crystal, a complex band parallel to the (010) plane is generated. The connection between two bands of this nature is facilitated by weak $H_2O\cdots H_2O$ interactions. The combination of water molecules involved in these interband interactions forms a nearly regular tetrahedron composed of four water molecules. This tetrahedral grouping is predominantly stabilized by electrostatic forces. Although the precise positions of hydrogen atoms within the studied minerals have not been experimentally determined, an overall understanding of the hydrogen bonding pattern can be derived from the description of the crystal structure and the wide range of O···O interatomic distances documented in crystallographic studies of symplesite and hörnesite,[16,38] which contributes to the observed spectroscopic features in the range of water OH stretching mode.

The infrared spectrum of hörnesite reveals a higher number of bands in both the H_2O stretching and bending regions compared to the symplesite spectrum (Fig. 6b). Two distinct bands arising from $\nu(H_2O)$ vibrations are observed at 3483 cm^{-1} and 3045 cm^{-1}, accompanied by two smaller peaks at 3401 cm^{-1} and 3166 cm^{-1} (Fig. 6b, Table 1 in Ref.[36]). The spectral pattern of OH stretching in hörnesite resembles the infrared bands observed in phosphate analogues such as vivianite (3460 cm^{-1}, 3281 cm^{-1}, 3104 cm^{-1})[39,40] and metavivianite (3350 cm^{-1}, 3240 cm^{-1}, 3145 cm^{-1}).[41]

In hörnesite, the bands corresponding to the bending modes of water molecules are situated at 1682 cm^{-1}, 1621 cm^{-1} and 1581 cm^{-1} (Table 1 in Ref.[36]), consistent with literature data.[42] These bands also closely align with the corresponding bands found in vivianite-type minerals, such as vivianite (1666 cm^{-1}, 1615 cm^{-1}, 1586 cm^{-1})[40] and metavivianite (1670 cm^{-1}, 1625 cm^{-1}, 1580 cm^{-1}).[41]

The discrepancies between the Raman spectra of hörnesite and symplesite are considerably more evident (Fig. 7).

It is important to note that, contrary to the three[42,43] to five[44] very weak Raman bands reported in the literature, which were attributed to water stretching vibrations, our Raman spectrum of hörnesite does not exhibit any bands in the water stretching region (Fig. 7b), aligning with the findings published by Frost et al.[45] This further confirms the well-known fact that the Raman technique is not sufficiently reliable in detecting the presence of water molecules in the analyzed samples, primarily due to their low polarizability. On the other hand, in symplesite, only one Raman band arising from water stretching vibrations was observed at 3448 cm^{-1} (Fig. 7a), in contrast to the two bands mentioned in the literature for parasymplesite.[42]

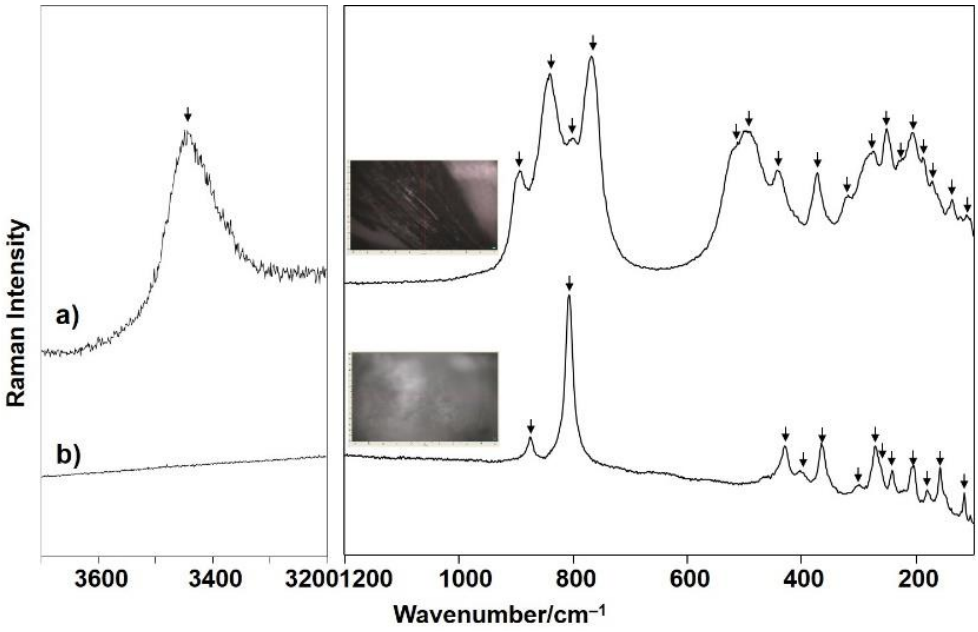

Fig. 7. Experimental Raman spectra of symplesite (a) and hörnesite (b). The peak maxima are marked with arrows. Pictures of the analyzed minerals under the micro-Raman objective are also given.

3.3. *Stibnite*

The far-infrared spectrum of stibnite [Sb_2S_3] (Fig. 8a) is very similar to the one reported in the

literature.[46,47] The bands at 372 and 337 cm^{-1} were assigned as Sb–S stretching vibrations (originating from the group with shorter Sb–S distances), while the bands at 276 and 242 cm^{-1} belonged to the stretching Sb–S vibrations originating from the group with the longer Sb–S distances.[48,49]

The bands below 200 cm^{-1} could be assigned to the S–Sb–S bending vibrations, as explained in our previous reports.[50] Similar far-IR spectra are observed for the series of other minerals also containing SbS_3 pyramids in their structures like pyrargyrite [Ag_3SbS_3], stibioellisite and weissbergite [$TlSbS_2$] (Fig. 8) and their identification could be, therefore, approached via far-IR spectra. However, when an approach was made to interpret the Raman spectra, the same mineral, regardless of being natural, synthetic crystals or nanoparticles, exhibited surprisingly different Raman spectrum to those reported in various literature sources. For instance, the Raman spectra of natural and synthetic stibnite [Sb_2S_3], collected by the use of green (514.5, 532 nm) and red (632.8 nm) excitation laser lines, portrays considerable differences to the works of Refs.[50–55] (Fig. 9). The much-pronounced differences in the Raman spectral view of stibnite, sometimes resulting in a completely different pattern, raises the question whether stibnite and its synthetic analogue, as well as other structurally similar SbS_3-pyramid-containing sulfosalts, undergo photoinduced transformation during spectral collection.

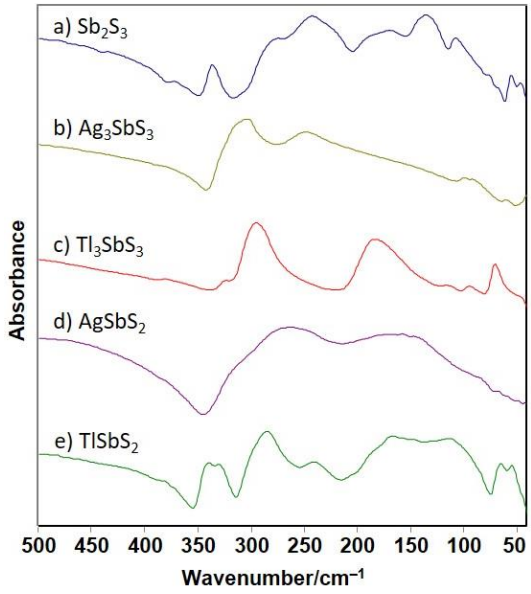

Fig. 8. Far-IR spectra of stibnite and other structurally related minerals containing SbS_3 pyramidal units

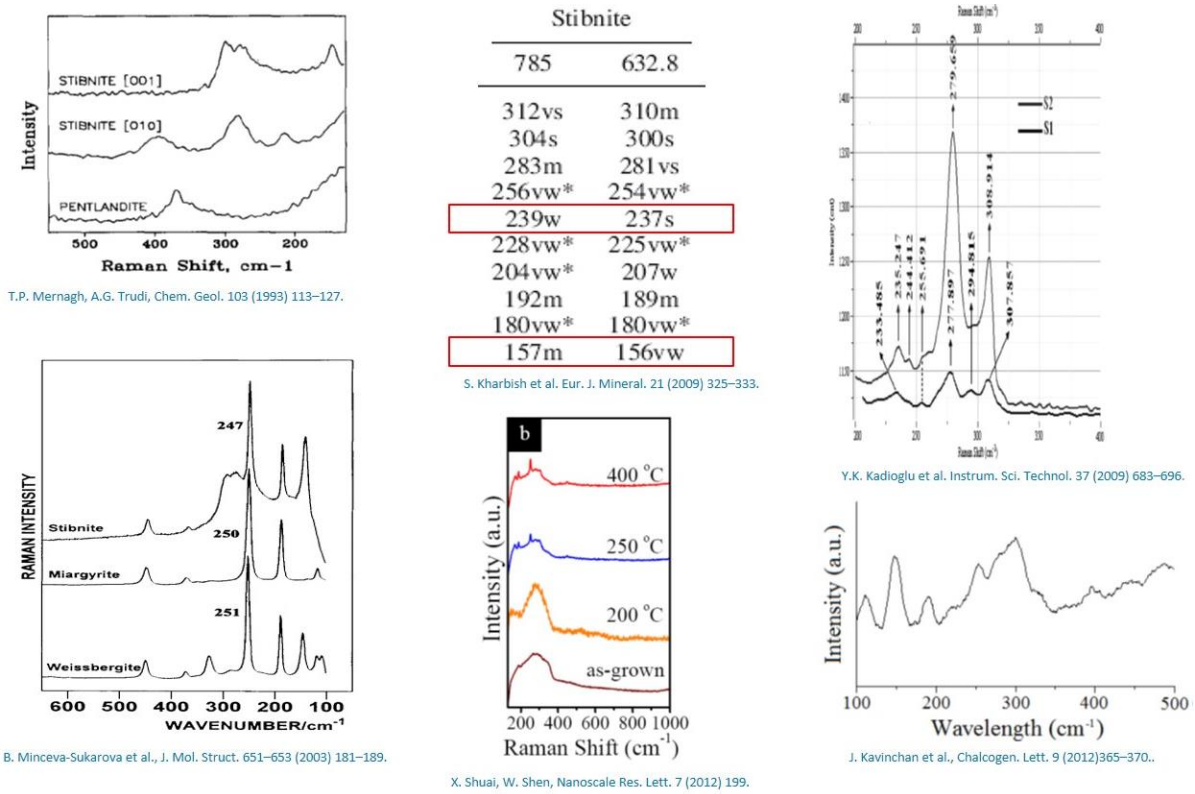

Fig. 9. Different views of the Raman spectra and the corresponding bands in stibnite [Sb_2S_3] from various literature sources

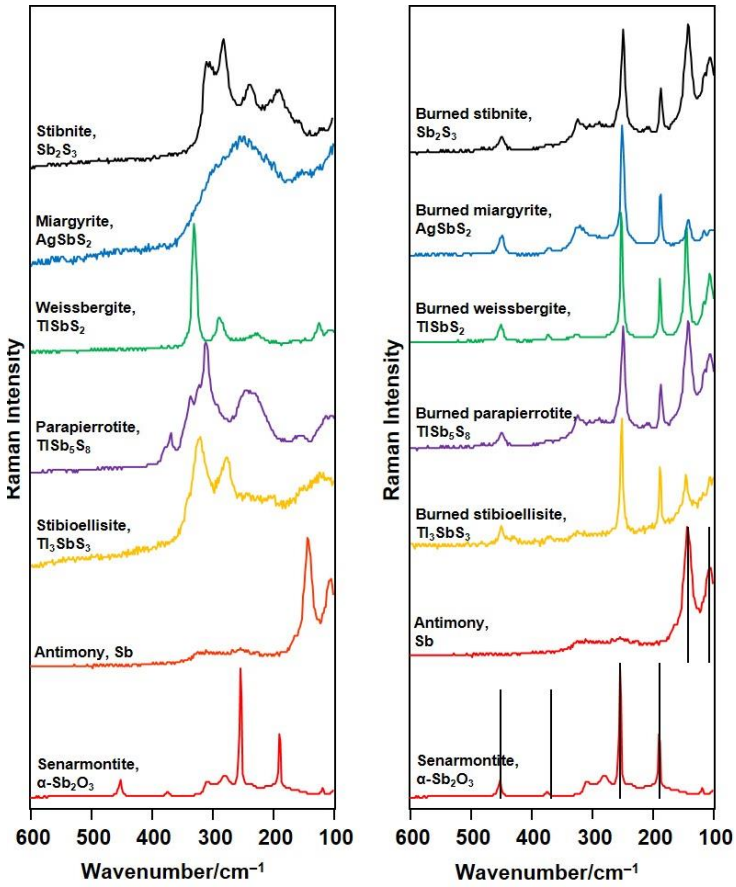

Fig. 10. Micro-Raman spectra of unburned (left panel) and degraded/burned samples of SbS_3-containing minerals (right panel). The degradation product is a mixture of antimony [Sb] and senarmontite [α-Sb_2O_3].

By comparing our obtained Raman results for stibnite with relevant literature sources, it becomes evident that a correct Raman spectrum of stibnite should exhibit two prominent bands centered around 280 cm^{-1} and 300 cm^{-1}. However, if the laser intensity is not properly controlled and increases beyond acceptable limits, the stibnite sample undergoes a transformation into senarmontite [α-Sb_2O_3] and antimony [Sb], resulting in intense peaks at 145 cm^{-1}, 184 cm^{-1} and 257 cm^{-1} (Fig. 10), which are attributed to these compounds.[56] The same photodegradation phenomenon is observed for other minerals that contain structurally related SbS_3 pyramids, including parapierrotite [$TlSb_5S_8$], stibioellisite [Tl_3SbS_3], miargyrite [$AgSbS_2$] and weissbergite [$TlSbS_2$] (Fig. 10). Consequently, if Raman spectra of light-sensitive sulfides containing SbS_3 pyramid structural units are recorded without carefully observing the specimen both before and after spectral collection in both in situ and ex situ measurements, erroneous conclusions and misidentifications may arise. Therefore, it is crucial to establish a proper protocol for collecting Raman spectra of laser light sensitive samples, paying close attention to the intensity of the laser power.

3.3.3. *Almandine*

To establish a connection between the vibrational and crystallographic characteristics of almandine, we present its IR absorption spectra within the wavenumber range of 1200 – 370 cm^{-1} (Fig. 11).[33] The identification process was based on the comparison of the spectral results with corresponding literature data for almandine specimens from various locations worldwide.[57–60] Since the studied mineral is natural, it is expected that some spectral differences may arise, making the identification process more challenging at times.

Nonetheless, the interpretation of IR bands proceeded smoothly within two distinct spectral regions. The first region encompassed bands above 800 cm^{-1} (998 cm^{-1}, 967 cm^{-1}, 901 cm^{-1}, 877 cm^{-1}), which were assigned as ν_3 modes originating from the SiO_4 tetrahedra.[33] An additional weak band was observed around 1090 cm^{-1}, consistent with synthetic analogues studied by Boffa Ballaran et al.[57] The second well-defined region combined peaks

from low-energy modes ranging from 700 to 400 cm^{-1}. The lowest band at approximately 450 cm^{-1} corresponded well with literature data and was attributed to the v_2 mode of the SiO_4 tetrahedra. The three highest bands in this spectral region of almandine (at 640 cm^{-1}, 571 cm^{-1}, and 530 cm^{-1}) also matched literature data, and they were attributed to the v_4 modes of the SiO_4 tetrahedra.[60] Furthermore, the band around 380 cm^{-1} was primarily assigned to SiO_4 rotations.

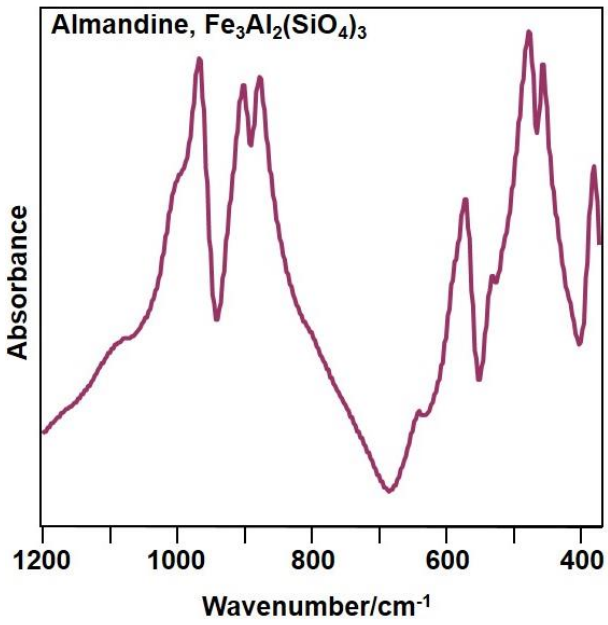

Fig. 11. Infrared spectrum of almandine from Staro Bonče

The unique Raman spectrum of the almandine mineral offers potential for its characterization.[59–64] In our study, we examined the almandine sample using various Raman instruments and excitation lasers (Fig. 12).[65] The upper spectral region, above 850 cm^{-1}, exhibited striking similarity to bands attributed to Si–O stretchings. The strongest band at 920 cm^{-1} was precisely assigned to the symmetric stretching mode of the SiO_4 tetrahedra. Additionally, three weak bands appeared in this region (at 838 cm^{-1}, 976 cm^{-1}, and 1025 cm^{-1}), corresponding to antisymmetric SiO_4 stretching vibrations. In the 650 – 450 cm^{-1} region, the Raman bands for almandine single crystals reported in the literature[59,60,62,64] associated with the bending v_2 and v_4 SiO_4 modes were observed at similar frequencies and intensities in our spectra.

However, there were two prominent bands at 446 cm^{-1} and 607 cm^{-1} that appeared only in the spectrum obtained using a 1064 nm laser. Initially, these unexpected bands were attributed to structural changes[33] resulting from possible sample photodegradation or burning during 1064 nm excitation. However, it was later discovered that these bands were actually caused by laser-induced fluorescence from the presence of rare earth element (REE) impurities in the specimen providing detailed explanation and theoretical background regarding their occurrence.[65]

This perplexing situation highlights the possibility of incorrectly assigning certain bands in FT-Raman vibrational spectra, which could lead to erroneous mineral identification. Similar observations have been made in other fields, such as cement minerals,[66] calcium minerals,[67–69] dental materials,[70] and bioceramics.[71] Understanding the geochemical behavior of REEs and the crystal chemistry of minerals exhibiting laser-induced REE fluorescence bands has expanded the knowledge of geological and biological samples.

Therefore, it is strongly recommended to view dispersive and FT-Raman spectroscopy, which belong to the same vibrational method (Raman), as complementary techniques rather than competing ones, as they each have their own advantages and limitations.

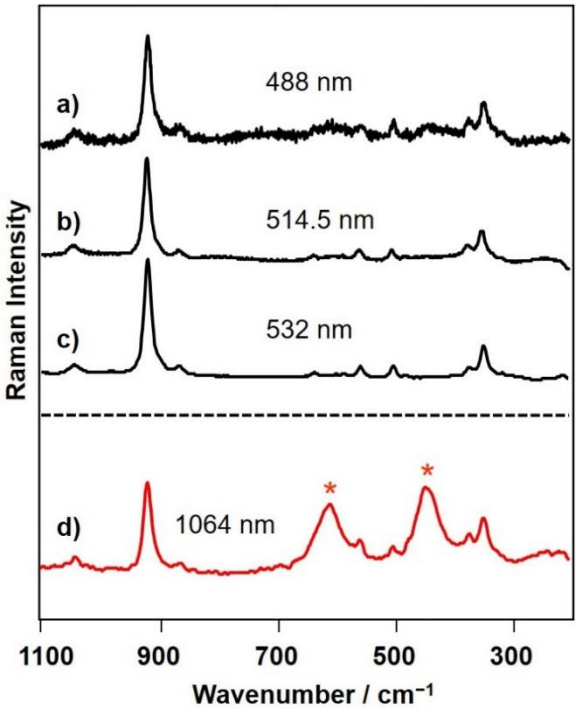

Fig. 12. Dispersive Raman spectra of almandine from Staro Bonče (a, b, c) obtained with 488, 514.5, and 532 nm excitation lines, respectively, as well as the FT-Raman spectrum (d) obtained with 1064 nm laser. The fluorescence bands in the latter spectrum at 446 and 607 cm^{-1} are marked.

3.3.4. *Realgar and pararealgar*

Light, as a natural phenomenon, has the ability to induce a wide range of physical and chemical changes in various minerals.[72–75] Several light-

induced effects have been observed in different minerals. Rutile can darken when exposed to light[75] while quartz varieties, including amethyst, can experience fading.[75–80] Fluorite may lose color and fluorescence,[75,79] and silver halides like chlorargyrite, bromargyrite, iodargyrite and miersite can undergo photodecomposition.[75] Proustite can undergo photooxidation.[75,79–81] However, the most notable influence is observed in the mineral realgar, which undergoes a structural change to its natural dimorph, pararealgar (Fig. 13). The photoconversion reaction, initially discovered by Douglas et al.[82] through XRD and SEM measurements, has been further investigated using various techniques. Infrared and Raman spectroscopy researchers have been particularly interested in studying the mechanism, propagation, side reactions, by-products, initiation conditions, rate, kinetics and light intensity threshold for conversion for over 30 years.[83–88]

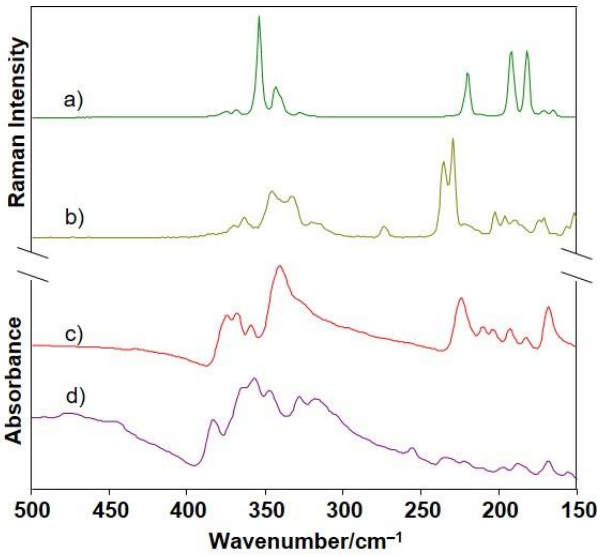

Fig. 13. Raman spectrum of the realgar (a) and the pararealgar (b) formed by the longer exposure to laser-excitation light on the starting mineral. The IR spectrum of the realgar (c) and the pararealgar (d) collected from realgar sample left for 3 years under natural light exposure.

As a result, the use of Raman spectroscopy instrumentation with visible excitation lasers, commonly employed for identifying and characterizing realgar in archaeological, cultural heritage and mineral studies, could inadvertently alter the chemistry of the analyzed sample and lead to misidentification, confusing realgar with pararealgar (Fig. 13). It has been discovered that this solid-state photoconversion can be triggered by light across the visible range and is not limited to safe light ($\lambda > 670$ nm). Therefore, infrared spectroscopy is recommended as the preferred vibrational spectroscopic technique for analyzing light-metastable and unstable mineral samples, even for remote and on-site studies, as it allows for the acquisition of experimental results without detecting sample-induced changes. Alternatively, near-infrared Raman spectroscopy instruments operating with either 785 nm or 1064 nm excitation lasers can be selected as another option.

3.3.5. *Jarosite*

Jarosite [$KFe_3(SO_4)_2(OH)_6$] and related subgroup sulfate minerals are of high importance in a variety of mineral processing demands, and the knowledge of jarosite formation mechanisms, its stability and thermal behavior is essential for its management and utilization.[89] Occasionally, during the processing of some minerals (e.g., zinc), jarosite is intentionally precipitated to remove unwanted iron, and this is known as the jarosite process.[90] In other mineral processing technologies (e.g., bioleaching of chalcopyrite), jarosite precipitates and forms unwanted passivating layers on ore minerals, which slows mineral dissolution and metal recovery.[91,92] However, the purity of this mineral is sometimes compromised because it occurs as a secondary product of the alteration of iron-rich minerals, and is formed and found in association with quartz, alunite and feldspar minerals, among others.[93] Therefore, it is of vital interest to screen jarosite tailing waste by effective and rapid techniques like infrared and Raman spectroscopy.[94] However, when interpreting the vibrational spectra of jarosite, it should be pointed out that infrared spectroscopy provides better insight into the associated quartz impurities in comparison to its Raman pattern (Fig. 14) mainly because the quartz infrared spectrum is much richer in bands compared to its Raman spectrum. Furthermore, there is a triplet of IR quartz bands (850 – 650 cm^{-1}) that appear in the spectral window that are neither overlapped by the sulfate and Fe–O vibrational band positions, nor overlaid with in-plane and out-of-plane OH vibrations (Fig. 14a,b).[94–104] On the other hand, the Raman spectrum of the same jarosite sample associated with the quartz impurities (Fig. 14c) shows only two bands attributed to quartz, but the strongest one (460 cm^{-1}) is almost completely overlapped by the higher wavenumber $\nu_2(SO_4^{2-})$ band centered at 454 cm^{-1} (Fig. 14c–e). Thus, if no particular attention is stressed, one might not determine the quartz impurity, particularly considering that the Raman spectra of minerals are sometimes only recorded down to 150 – 200 cm^{-1} (Fig. 14d)[105] however the second band from the quartz impurity does not appear until 120 cm^{-1}.

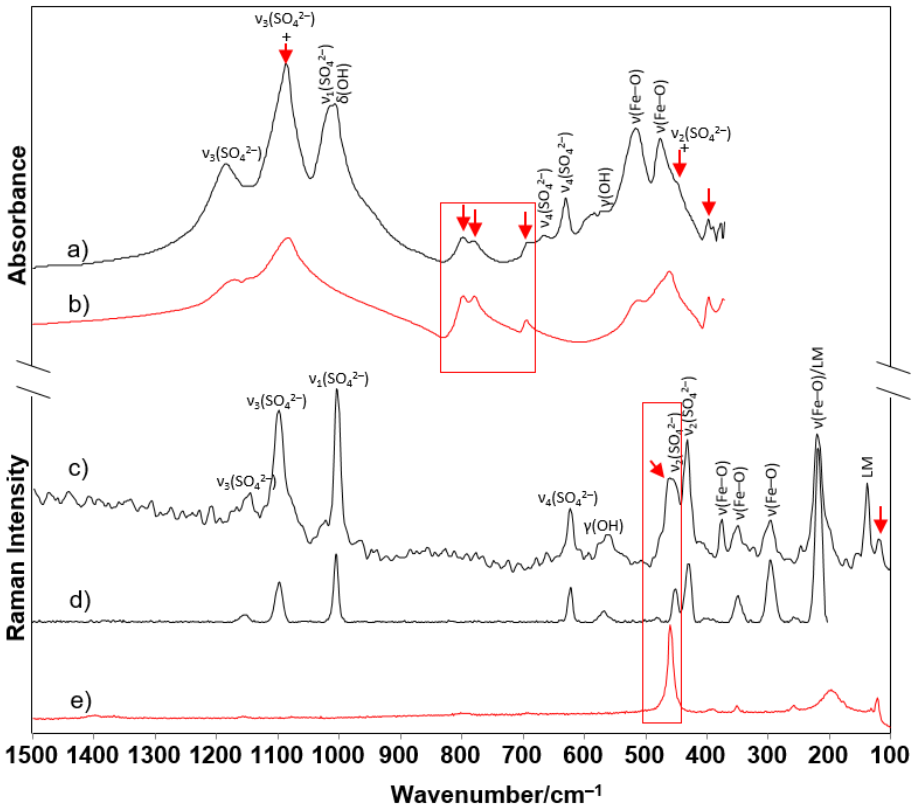

Fig. 14. Infrared spectrum of jarosite from Bukovik (a) and the corresponding spectrum of quartz (b). Raman spectrum of the analyzed jarosite from Bukovik (c), compared to the spectrum of pure jarosite, (RRUFF ID: X050105) (d),[105] and quartz (e). The rectangular fragments mark the region of interest for the appearance of the bands originating from the quartz impurities (marked by arrows).

3.3.6. *Struvite*

The formation of some minerals does not exclusively occur during geological processes, as they might appear as urinary calculi during different biochemical reactions that take place in the human body. Although literature enlists pharmaceutical products known for their ability to form calculi,[106] the majority of more than a hundred known urinary calculi are composed of minerals. The need to reveal the chemical composition and identify the type of urinary stone, makes vibrational (IR and Raman) spectroscopy the first choice technique capable of providing accurate results in a rapid, cheap, nondestructive, and environmentally friendly manner. Nonetheless, Raman spectroscopy confronts specific constraints, with the most prominent one being the issue of background fluorescence that can obscure the entire spectral range, rendering Raman bands nearly impossible to discern.[107] Typically, the principal source of fluorescence stems from impurities present, particularly in biological samples.[108] The interference caused by fluorescence is also dependent on the laser excitation wavelength. Therefore, selection of the correct excitation source as well as computational, photo, or chemical bleaching can be used in order to avoid fluorescence background noise in the Raman spectrum.[109–112] However, these preprocessing methods and algorithm tools may be time intensive, laborious and utilizes consumables. Therefore, IR spectroscopy stands as a more convenient method for analysis of urinary stones due to the lack of spectral fluorescence. Furthermore, the minerals/calculi containing structural water molecules can additionally provide stronger bands in the corresponding IR spectrum. On the other hand, the water molecules, being a part of the crystalline structure in some urinary calculi minerals, are weak Raman scatterers and their Raman active modes do not provide strong spectral signals making the identification process even more difficult.

Here, we present the advantage of using IR spectroscopy to accurately identify the struvite [$MgNH_4PO_4 \cdot 6H_2O$] mineral that very frequently occurs in urinary calculi. Despite the large number of different compositional molecular units (NH^{4+}, PO_4^{3-}, H_2O), its Raman spectrum is scarce in bands (Fig. 15c) and shows fluorescence. On the other hand, its infrared spectrum clearly distinguishes various regions typical for the vibrations of the molecular units (Fig. 15a,b).[113–119] Raman spectra

identification[117–121] is even more challenging if the spectrum is collected in a shorter exposure time since only three bands from the phosphate vibrations are evident, without the appearance of any Raman bands from the ammonium ions. Thus, the strong fluorescence and weak bands might compromise the identification of struvite among the other possible phosphate-built urinary calculi candidates (monetite, brushite, newberyite, dittmarite).

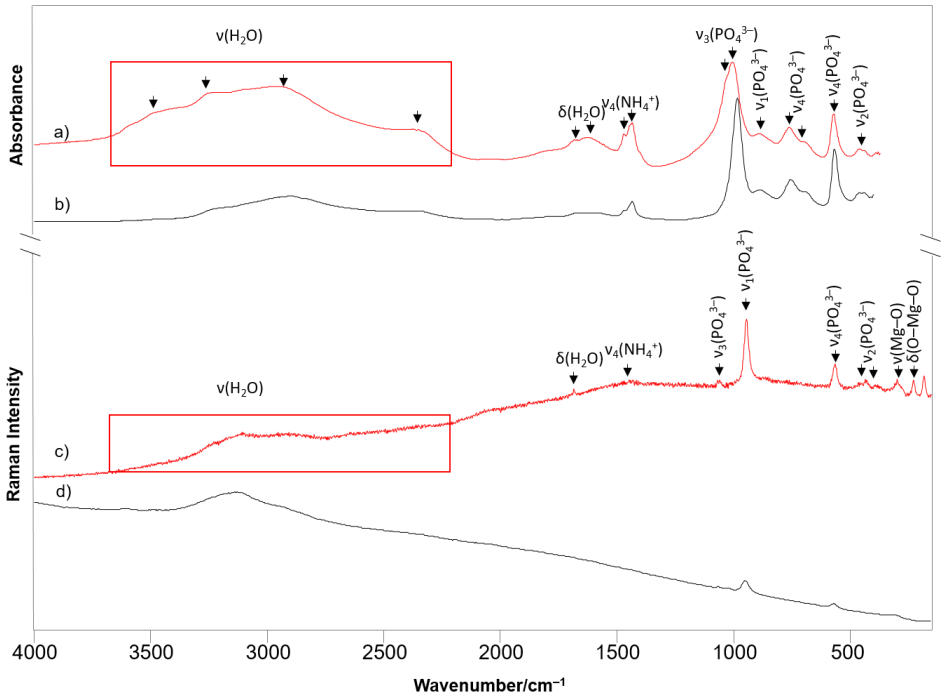

Fig. 15. Infrared and Raman spectrum of struvite (a, c) and the corresponding spectra from the literature, (RRUFF ID: R050511) (b, d).[105] The assignment of the marked bands from the NH_4^+, PO_4^{3-} and H_2O vibrations is given by arrows, whereas the region for the ν(H_2O) vibrations is marked.

3.4. *Raman spectroscopy dominance over infrared spectroscopy*

3.4.1. *Pharmacolite, picropharmacolite and vladimirite*

These minerals, in addition to the presence of crystalline water, all contain hydrogen arsenate units. The pharmacolite [$Ca(AsO_3OH)\cdot 2H_2O$] mineral contains only hydrogen arsenate units, whereas vladimirite [$Ca_4(AsO_3OH)(AsO_4)_2\cdot 4H_2O$] and picropharmacolite [$Ca_4Mg(AsO_3OH)_2(AsO_4)_2\cdot 11H_2O$] additionally contain arsenate building blocks in the crystal structure. Considering the diverse compositional and structural complexity of the minerals, it was interesting to test the capability of infrared and Raman spectroscopy to determine and assign the bands that arise from either the hydrogen arsenate or the arsenate structural anions. Despite the fact that all studied minerals manifest OH vibrations, it was not of particular interest here to evaluate the behavior of these vibrations along with the water vibrations in the spectral regions typical for the stretching and the bending vibrations of these oscillators, although these considerations were undertaken in our previous work.[122]

The infrared spectra in the range of 1000 – 450 cm^{-1} exhibit a complex pattern of overlapping bands, which can be attributed to vibrations originating from $(AsO_3OH)^{2-}$ and/or $(AsO_4)^{3-}$ groups. All the minerals studied share distinct spectral similarities in the 950 – 750 cm^{-1} range (Fig. 16a–c), where the stretching modes give rise to characteristic bands. It is reasonable to propose that the indistinct band observed at 934 cm^{-1} in pharmacolite corresponds to the ν_3 mode associated with $(AsO_3OH)^{2-}$ units, which aligns very well with the findings obtained from our theoretical computations (see Table 2[122]). A similar band at 938 cm^{-1}, attributed to the ν_3 mode, also appears in dussertite [$BaFe^{3+}{}_3(AsO_4)(AsO_3OH)(OH)_6$].[123] The subsequent bands, displaying a strong and prominent intensity around 900 and 860 cm^{-1} in all three minerals, can be assigned to the ν_3 modes originating from $(AsO_3OH)^{2-}$ and/or $(AsO_4)^{3-}$ groups. The intense band situated within the 810 – 800 cm^{-1} re-

gion can be ascribed to the v_3 mode originating from the protonated arsenate group,[124] while the weak band around 845 cm^{-1} is attributed to the corresponding v_1 mode (see Table 2[122]), consistent with theoretical calculations. However, due to the broad manifestation of the stretching bands, the IR spectroscopy alone cannot precisely determine whether the bands in this region of vladimirite and picropharmacolite spectra result from stretching vibrations within the AsO_4 units or the AsO_3OH units. Additionally, despite the presence of both unit types in the latter two minerals, the number of bands in this spectral region is not greater compared to the pharmacolite spectrum, where AsO_3OH units alone are present in the structure.

The v_4 modes originating from AsO_4 and AsO_3OH units consistently appear within the 480 – 450 cm^{-1} range in all minerals, and their positions remain practically constant (Table 2[122]). Therefore, the IR spectra below 500 cm^{-1} do not provide useful information for differentiating between these hydrogen arsenate minerals (see Fig. 16a–c). These interpretations were consistent with the IR/Raman spectra of other structurally similar hydrogen arsenate salts.[125–127]

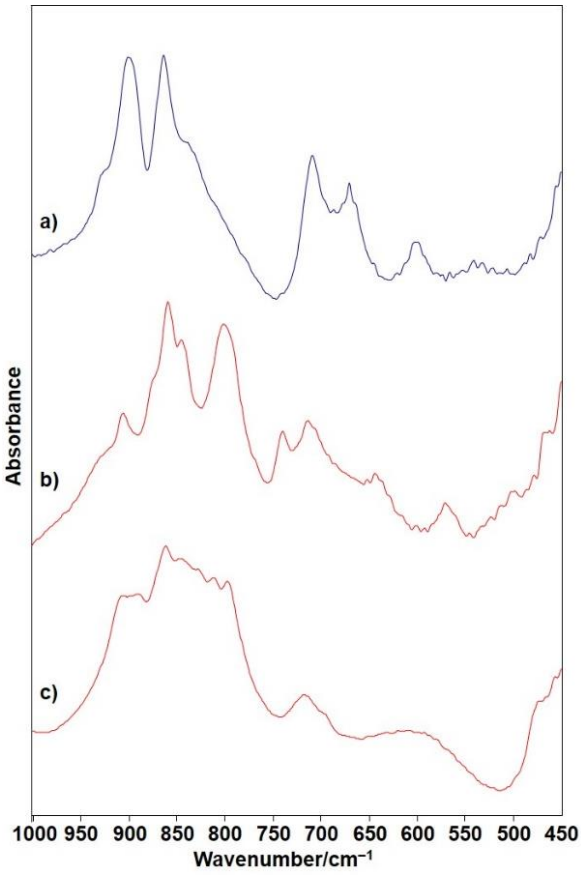

Fig. 16. IR spectra of pharmacolite (a), vladimirite (b) and picropharmacolite (c) depicting arsenate bands from AsO_3OH and AsO_4 units

In contrast, the Raman spectra of these three minerals below 1000 cm^{-1} provide a clear representation of the distinct presence of the crystallographic AsO_4 and AsO_3OH units in their structures, making it possible to deduce the number of these units in each mineral (see Fig. 17). Consistent with numerous published articles on the Raman behavior of hydrogen arsenate minerals,[123,124,128–133] the higher wavenumber bands are attributed to the antisymmetric $v_3(AsO_3OH)$ modes, followed by one or two stronger bands originating from the symmetric $v_1(AsO_3OH)$ modes at slightly lower wavenumbers. In the case of the pharmacolite mineral, which consists of structurally equivalent $(AsO_3OH)^{2-}$ units,[134] these bands were observed at 891, 862 and 841 cm^{-1} (see Fig. 17a), closely resembling their positions in the available literature data.[134] On the other hand, the Raman spectra of vladimirite and picropharmacolite reveal the presence of three sets of two bands (six bands in total) within the 925 – 775 cm^{-1} range (see Fig. 17b, c), which fully correspond to the existence of three non-equivalent symmetric AsO_4 groups (one of which is protonated) in the structures of vladimirite and picropharmacolite. Specifically, the two highest wavenumber bands in the spectra of both minerals can be attributed to the v_3 and v_1 vibrations originating from the hydrogen arsenate group, while the lower wavenumber sets of two bands are assigned to v_1 and v_3 modes from the structurally in Ref.[122]) (Fig. 17b,c). Additionally, the well-resolved lower wavenumber band at 708 cm^{-1} in the pharmacolite spectrum, as well as the broad and weak bands at 760 cm^{-1} (vladimirite) and 720 cm^{-1} (picropharmacolite), are attributed to the ν(As–OH) modes.[134,135]

The aforementioned significant findings remain consistent when examining the lower wavenumber bands (500 – 335 cm^{-1}, Fig. 17) derived from the corresponding v_2 and v_4 modes (Table 3 in Ref.[122]). In the case of pharmacolite, the bands at 450 and 368 cm^{-1} can be attributed to the vibrations of $v_4(AsO_3OH)$ and $v_2(AsO_3OH)$, respectively, aligning perfectly with our theoretical results for this system (see Fig. 17a).[122] Conversely, in the spectra of vladimirite and picropharmacolite, we observed six bands originating from the AsO_3OH unit and both (AsO_4) units (three sets of two bands) (see Fig. 17b and 17c). It is expected and observed that the v_2 bands exhibit stronger intensity compared to the v_4 bands in the spectra of all three minerals. It is worth mentioning that previous literature on vladimirite did not focus on precisely attributing the bands in this region, providing either stretching ($\nu_1 + \nu_3$) or bending ($\nu_2 + \nu_4$) charac-

teristics of the resulting bands.[135] Additionally, the quality of the picropharmacolite Raman spectrum[136] was low and did not allow for the extraction of relevant spectra-structural information.

To offer a firmer theoretical basis as well as a support for the tentative assignment of bands in the vibrational spectra, quantum theoretical calculations within the density functional theory (DFT) framework have been performed. As discussed further, theoretical calculations in the present case have allowed a few reassignments of bands appearing in the OH stretching region.

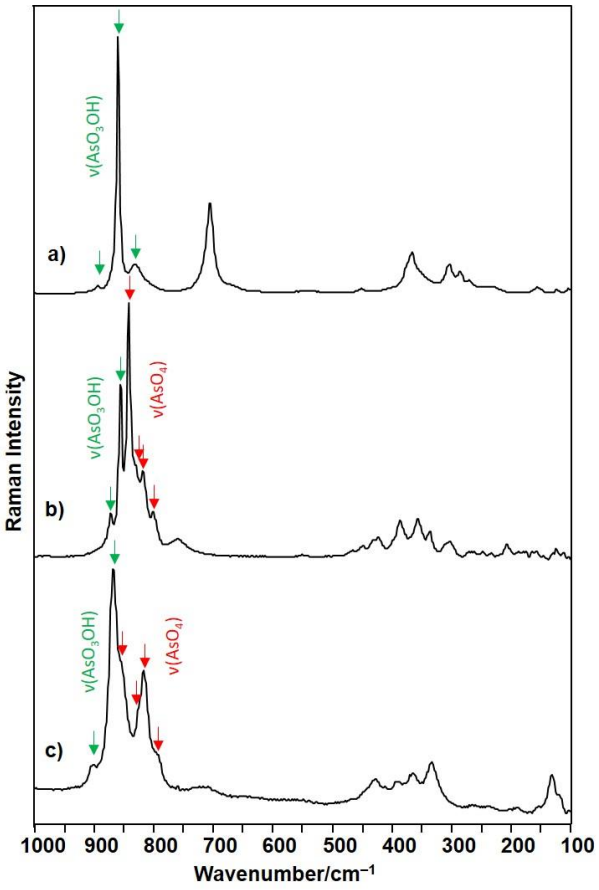

Fig. 17. Raman spectra of pharmacolite (a), vladimirite (b) and picropharmacolite (c) depicting arsenate bands from AsO_3OH and AsO_4 units. Only the bands from the stretching vibrations of these units are marked in different color.

Two theoretical approaches, both of which are based on the periodic density functional theory (DFT) within the framework of the Kohn-Sham formalism, have been actually implemented. The first approach is the pseudopotential plane-wave (PSPW) density functional methodology (PSPW DFT), as implemented in the NWCHEM series of codes, while the second one is based on expansion of single particle wavefunctions (the "crystalline orbitals") as linear combinations of Bloch functions. Bloch functions are, themselves, defined through local functions (atomic orbitals). Local functions are actually linear combinations of Gaussian-type functions, with exponents and coefficients optimized for solid state calculations. The second, localized basis function approach is the one implemented in the CRYSTAL series of codes. By carrying out numerous test computations based on PSPW DFT in the present study, it was found that the most reliable and physically acceptable results in the case of pharmacolite were obtained with the nonlocal DFT approach, within the generalized gradient approximation (GGA), employing the parameter-free PBE0 exchange-correlation functional. Note that the PBE0 functional has been constructed combining the PBE generalized gradient functional with a predefined amount of exact exchange. In the case of vladimirite, however, acceptable convergence was obtained only within the local density approximation (LDA), i.e., using Vosko's functional. To represent the wavefunctions of the valence electrons, these were expanded in the plane-wave basis set. To describe the interaction of the valence electrons subsystem with the remaining part of the system (nuclei + core electrons), a norm-conserving Haman pseudopotential for As atoms, parametrized Haman pseudopotentials for O and H, as well as Troullier-Martins pseudopotentials for Ca were used. To obtain physically reliable productive results, an extensive series of initial testing computations have been carried out; for the final productive computations, 32 × 32 × 32 grid of points was used for discretization along lattice vector directions, while Ewald summation in each spatial direction was carried out over eight unit cells. The atomic positions within the unit cells of the title systems were optimized with the Grassman LMBFGS energy minimization scheme. Unit cell parameters were, however, kept fixed at the experimentally determined values. To compute the nuclear Hessian, an analytical approach that relied on finding the first derivatives of analytic gradients at the located stationary points on the explored potential energy hypersurfaces was used. To subsequently compute the harmonic vibrational frequencies, the mass-weighted Hessian was diagonalized. Translations and rotations of the nuclear Hessian were projected out by Eckart's projection algorithm.

Another variant of DFT successfully applied to the case of pharmacolite mineral in the present study was based on localized basis sets of a Gaussian type orbitals (GTO), was also successfully applied. The basis set used for Ca was based on the

representation of core electrons by the Hay-Wadt effective core potential (ECP) plus 3-1(1d)G contracted sp-type shells; for As the Durand-type ECP for core electron subsystem plus 2-1(1d)G on remaining electrons was used; for O atoms, the 8-411 basis set was used, while for H atoms the 3-1p1G one. To construct the Kohn-Sham Hamiltonian, a combination of Becke's three-parameter adiabatic connection exchange functional (adopting the WVN 5 functions, B3) with the Lee-Yang-Parr (LYP) correlation functional was used. Control of the calculation of two-electron Coulomb and exchange integrals, the truncation criteria for the infinite sums encountered in the calculations, etc., was achieved by the following set of TOLINTEG parameters T1 – T5: 7, 7, 7, 7, 16. Regular sublattice with shrinking factor 6 was used to sample the reciprocal space; this corresponds to 80 independent k-points in the irreducible Brillouin zone (BZ). For numerical integration in DFT, the pruned grid of 75 radial and 974 angular points (75,974) was used. Optimizations of atomic positions were carried out using analytical energy gradients with respect to atomic coordinates. Convergence criterion for SCF KS equations on total energy was set to 10^{-7}. Subsequent to geometric optimizations, harmonic vibrational analysis of the system was carried out at the Γ-point. The dynamical matrix was computed by a numerical calculation of the derivatives of analytically computed atomic gradients. Harmonic vibrational frequencies in the normal-mode approximation have been further computed by diagonalization of the mass-weighted dynamical matrix, while IR intensities were computed through the atomic Born effective charge tensors, evaluated by a Berry phase methodology. Raman intensities were computed by calculation of the corresponding Raman tensor elements and subsequent simulation of the situation encountered in a powdered sample by computation of integrals over all possible orientations of ideal bulk crystals and reducing these integrals to the three rotational invariants.

Among other results, the theoretical calculations in the present study have implied the possibility of somewhat different assignment of bands appearing in the region of OH stretching modes. Namely, periodic DFT results favor an assignment of the two highest spectral bands to the OH stretching modes of weakly bonded OH oscillators of the crystalline water molecules (~3525 and 3444 cm^{-1} in the IR spectra of pharmacolite), and a possible contribution to the OH stretching region by hydrogen arsenate species (i.e., of the OH oscillators within these groups) at somewhat lower wavenumbers (up to ~3200 – 3250 cm^{-1}, e.g., in the case of pharmacolite). Such assignment seems to be in line with a more detailed analysis of the crystal structure of minerals like pharmacolite, where rather weak hydrogen bond contacts exist between crystalline water molecules. This reassignment is further supported by the results of the TGA-DTA analyses. At the same time, the acidic proton within the hydrogen arsenate groups takes part in rather stronger hydrogen bonds within the general in-crystal noncovalent bonding pattern. Certainly, this issue appears to be rather interesting from a theoretical point of view; it tackles questions such as the influence of a polarizing environment on molecular subunits containing acidic protons in relation to the position of the corresponding OH stretching band. It is worth noting in this context that theoretical assignment of other bands in this spectral region is in line with the expectations based on previous spectroscopic data.[122] While the GTO variant of periodic DFT does not predict appearance of OH stretching bands at as low as ~2330 in the case of pharmacolite, the PSPW KS approach actually does predict significant IR absorption due to OH oscillators at such lower wavenumbers.

3.5. *Powder XRD dominance over single-crystal XRD*

3.5.1. *Symplesite*

Microcrystalline minerals often have very small crystal sizes, which can make it difficult to determine their crystal structures using a single crystal XRD technique. For such scenarios, an X-ray powder diffractometer (XRPD) is a powerful tool used for solving their structures because it can provide information about the average crystal structure of a sample without the need for single crystals. One example for such a structurally elusive mineral is the very rare symplesite [$Fe_3(AsO_4)_2{\cdot}8H_2O$], discovered in the late 19th century, whose crystal structure was vividly debated. First, its unit cell was presented as a monoclinic crystal system.[137] About a half century later, a triclinic symmetry was postulated,[138] whereas later[139,140] its symmetry was reiterated as monoclinic, with *C*2/*m* space group reporting its unit cell parameters. In 1954, Ito corrected his previous reports,[141] realizing that the study was actually performed on a sample of the monoclinic dimorph, parasymplesite [isostructural to vivianite, $Fe_3(PO_4)_2{\cdot}8H_2O$] and announced a follow-up study that would report the crystal structure of symple-

site. To the best of our knowledge, the only crystallographic study to be reported ever since, was by Schmetzer et al.[142] only confirming the triclinic symmetry. This is one example of many similar timeline reports dealing with the intricacy of solving the crystal structure of microcrystalline, very rare secondary minerals, whose growth occurs in complex association with other minerals in the oxidized zone of arsenic-rich hydrothermal deposits.

To overcome such structural problems, the crystal structure of natural symplesite was refined by high-resolution X-ray powder diffraction (XRPD) laboratory data collected from very pure material.[36] Thus, the crystal structure of symplesite can be explained by the positioning of one iron atom at the center of inversion (Fe1, site multiplicity 1) and the second iron atom at a general position (Fe2, site multiplicity 2). The Fe1 atom is coordinated by four oxygen atoms from the water molecules and by two oxygen atoms from the arsenate group forming a slightly distorted octahedron with composition $[Fe^{II}O_2(H_2O)_4]$ (Fig. 18a). The Fe2 atom forms inversion symmetry related Fe2–Fe2 doublets spaced at 3.118 Å (Fig. 18b).

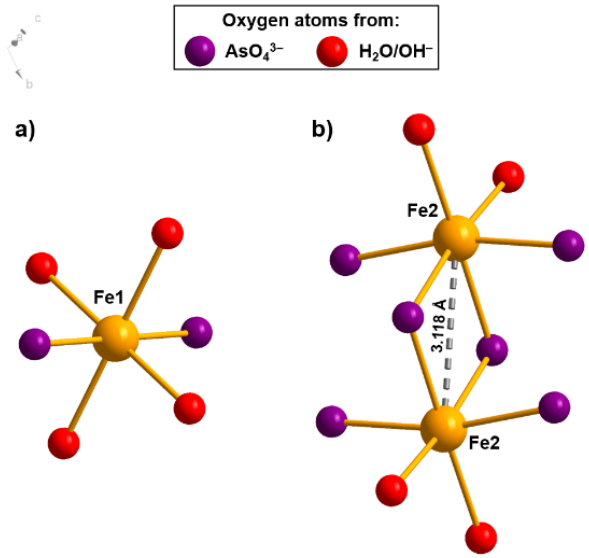

Fig. 18. Coordination sphere around the (a) Fe atom positioned at the center of inversion and (b) Fe atom occupying a general position in the unit cell of symplesite

The coordination sphere around the Fe2–Fe2 doublet consists of two edge-sharing octahedra. To each octahedron, the arsenate groups contribute four oxygen atoms (two oxygen atoms being shared between both iron cores). The remaining two oxygen atoms can be attributed to either water molecules and/or to hydroxide anions because the intrinsic limitations of the XRPD method does not allow unambiguous determination of the positions of hydrogen atoms and the atomic charge. Nevertheless, the positions of all non-hydrogen atoms in the symplesite crystal structure were refined by XRPD.[16] Thus, if it is assumed that symplesite is isostructural to metavivianite,[41] the chemical formula of the former mineral should be corrected. The chemical formula of the Fe2–Fe2 double octahedra should be $[Fe_2^{III}O_6(H_2O/OH)_4]$ and not $[Fe_2^{II}O_6(H_2O)_4]$ and a mixed valence nature of symplesite, analogous to that of metavivianite, can only be suspected.

4. CONCLUSIONS

Vibrational spectra and X-ray powder diffraction patterns allow rapid verification of the mineral and its purity and are usually the first choice for unambiguous identification of the sample under study. The major problems that may be encountered in this process are:

i. The presence of mineral impurities (> 1 wt%);

ii. The possible laser-induced decomposition/degradation/conversion of the sample or the appearance of fluorescence during Raman spectral acquisition;

iii. Insufficient sample quantity for analysis when dealing with rare-occurring minerals;

iv. The need to powder or destroy the sample in order to perform quantitative transmission IR measurements and/or X-ray powder diffraction experiments.

Therefore, depending on the initial requirements, it is of utmost importance to select the most suitable technique among IR, Raman spectroscopy and X-ray powder diffraction for mineral identification and characterization. We have listed here some examples where one of the techniques used outperforms the other(s), displaying their advantages and limitations regarding the studied minerals (Table 5).

More specifically, the following conclusions were drawn for the reported case studies:

i. The problem of particle size of crystallites of minerals (rutile) with high refractive index leads to an abrupt difference between the acquired infrared spectra.

ii. Depending on the wavelength of laser excitation, the Raman spectra of the same mineral (almandine) may exhibit additional unexpected bands that could be incorrectly assigned to the fundamental Raman bands. This leads to incorrect conclusions in mineral identification.

iii. Laser excitation provokes photodegradation (stibnite) or even conversion of the photosensitive minerals to other varieties (realgar-pararealgar conversion).

iv. The XRPD technique has been shown to be more reliable in detecting the presence of various types of impurities in minerals (hematite), especially those absorbing in the far IR region (oxides, sulfides). In this infrared region, the registration of the bands from the other oxygen-containing minerals (carbonates, sulfates, phosphates, arsenates, vanadates, arsenates, silicates, etc.) present as impurities and can barely be detected due to their weak manifestation.

v. The nominally anhydrous minerals (beryl), which can accommodate water and/or hydroxyl ions in the cavities of the crystal structure, should be studied by vibrational spectroscopy techniques (particularly IR spectroscopy) because XRPD cannot detect these molecules.

vi. Special care should be taken to determine and identify the contaminants in the case of the two- (or multi-) component mineral samples or samples with impurities as sometimes even their strongest impurity bands are overlaid with the bands from the dominant phase making them difficult to be traced. In such scenarios, both infrared and Raman spectroscopy should be used simultaneously as quartz as impurity was hardly detected in the Raman spectrum of contaminated jarosite sample.

vii. Sharp and intense Raman bands can be very informative and helps to distinguish between the hydrogen arsenate and arsenate units, since the bands of these units are overlapped or overlaid and not easily separated in the IR spectrum.

viii. The Raman spectra of minerals that build urinary calculi might show fluorescence resulting in ambiguous and problematic identification of the stone as some of the major Raman bands can be obscured, as shown in the case of struvite.

ix. The structure of microcrystalline minerals (symplesite) must be solved by Rietveld refinement using the XRPD data since no single crystals are found in nature.

e 5

A matrix that correlates each mineral with the investigated techniques attributing them different grades in accordance with their affinity (1 – most suitable; 2 – suitable; 3 – least suitable/not possible)

Type of affinity	Studied minerals	Infrared spectroscopy	Raman spectroscopy	X-ray powder diffraction
Mineral impurities detection threshold	Hematite, Rutile, Jarosite	2	3	1
Fluorescence	Almandine, Struvite	1	3	1
Water in minerals	Beryl, Hörnesite, Symplesite	1	2	3
REE traces in minerals	Almandine	3	1	3
Light-sensitive minerals	Realgar, pararealgar, parapierrotite, stibnite	1	3	1
Minerals with complex chemical composition	Picropharmacolite, Pharmacolite, Vladimirite	2	1	3

Funding: This research received no funding.

Acknowledgments: The authors thank Professor Blažo Boev from Goce Delčev University, Štip, N. Macedonia for providing some of the studied samples.

Conflicts of interest: The authors declare no conflict of interest.

REFERENCES

Quantitative mineralogical analysis using the Rietveld full-pattern fitting method, *Am. Mineral*. **1993**, *78*, 932–940.

Modern X-ray diffraction methods in mineralogy and geosciences, *Rev. Mineral. Geochem*. **2014**, *78*, 1–31.

(3) A
l
i
,
A
.
;

tion: A review for engineers of the fundamentals, applications, and research directions, *Minerals* **2022**, *12*, 205. https://doi.org/10.1007/s002690050097

C. (Ed.), *The Infrared Spectra of Minerals*, Mineralogical Society of Great Britain and Ireland, London, **1974**.

Raman Spectroscopy of Minerals. In: *The Infrared Spectra of Minerals*; Farmer, V.C. (Ed.). Mineralogical Society of Great Britain and Ireland, London, **1974**, 119–135.

Infrared and Raman Spectroscopy. In: *Spectroscopic Methods in Mineralogy and Geology*; Hawthorne, F.C. (Ed.), De Gruyter, Berlin, **1988**, *18*, 99–160.

Library of FT-Raman spectra of pigments, minerals, pigment media and varnishes, and supplement to existing library of Raman spectra of pigments with visible excitation, *Spectrochim. Acta Part A* **2001**, *57*, 1491–1531.

https://doi.org/10.1016/S1386-1425(00)00495-9

(8) M
a
https://doi.org/10.1016/S0924-2031(02)00065-6

(9) J
o
v
a
n
o
y
s
k
i
;
(10) Yin, Y.; Jin, J.; Zhang, W.; Tian, H.; Hu, Z.; Yuan, M.; FTIR techniques in clay mineral studies, *Vib. Spectrosc.*, **2003**, *31*, 1–10.

(11) P
e
t
k
o
v
M
a
u
s
https://opengeology.org/Mineralogy/12-x-ray-diffraction-and-mineral-analysis/ (accessed on 5 April 2024)

Tinaksite and tokkoite: X-ray powder diffraction, optical, and vibrational properties, *Crystals* **2022**, *12*, 377. https://doi.org/10.3390/cryst12030377

Minerals from Macedonia. XXX. Complementary use of powder transmission infrared spectroscopy (FTIR) in the gemological field, *N. Jb. Miner. Abh.* **2019**, *196*, 215–243. https://doi.org/10.1127/njma/2019/0847

HYPERLINK https://opengeology.org/Mineralogy/12-x-ray-diffr

American Gem Trade Association (AGTA), **2019**, 2. Available online: https://agta.org/advantages-and-disadvantages-of-raman-fourier-transform-infrared-spectroscopy-ftir-in-the-gemological-field/ (accessed on 5 April 2024)

Laboratory techniques in experimental petrology, *N. Jb. Miner. Mh.* **1971**, 450–459.

L.; Gržetić, I., Thallium-containing mineral systems. Part II: Thallium and silver sulfosalts with applications to polymetallic ores, *Chem. Erde-Geochem.* **1993**, *53*, 273–288.

FT-IR and micro-Raman spectroscopic characterization of minerals in high-calcium coal ashes, *J. Energy. Inst.* **2018**, *91*, 389–396. https://doi.org/10.1016/j.joei.2017.02.003

(16) Kuncevski, I.; Makreski, P.; Dimitrieski, R. Z.; Jovanovski, G.; Gajović, A.; Tanaskovska, S.; Minceva-Sukarova, B.; Soptrajanov, B., The crystal structure of symplesite, *Z. Anorg. Allg. Chem.* **2015**, *641*, 1207–1210. https://doi.org/10.1002/zaac.201500181

(17) V
a
n
d
e
r
b
i
l
t
;
Generalized norm-conserving pseudopotentials, *Phys. Rev. B* **1989**, *40*, 2980–2987. https://doi.org/10.1103/PhysRevB.40.2980

(19) K
l
e
i
n
m
a
n
;
(20) L
i
n
d
b
e
r
g
,
G
.
;
In: *Mineralogy - Free Textbook for College-Level Mineralogy Courses*, Second Edition, University of North Dakota, **2022**. Available online:

Efficient pseudopotentials for plane-wave calculations, *Phys. Rev. B* **1991**, *43*, 1993–2006. https://doi.org/10.1103/PhysRevB.43.1993

Infrared and Raman spectra of inorganic solids–state of the art, *Trends Appl. Spectrosc.* **1998**, 2, 59–88.

Variations of the infrared powder spectra of TiO_2 and SnO_2 (rutile) with polarization, *Spectrochim. Acta Part A* **1991**, *47*, 765–774. https://doi.org/10.1016/0584-8539(91)80148-C

Infrared absorption study of metal oxides in the low frequency region (700–240 cm^{-1}), *Spectrochim. Act*, **1964**, *20*, 799–808. https://doi.org/10.1016/0371-1951(64)80079-5

(25) L
u
x
o
n
Infrared surface modes in corundum-type microcrystalline oxides, *Spectrochim. Acta Part A* **1982**, *38*, 797–802. https://doi.org/10.1016/0584-8539(82)80070-6

(27) Makreski, P.; Jovanovski, G.; Kaitner, B.; Stafilov, T.; Minerals from Macedonia. X. Separation and identification of some oxide minerals by FT IR spectroscopy, AAS, AES-ICP and powder XRD, *N. Jb. Miner. Abh.* **2004**, *180*, 215–243. https://doi.org/10.1127/0077-7757/2004/0180-0215

(28) P
e
t
j
k
o
v
Interpretation of the infrared absorption spectra of stannic oxide and titanium dioxide (rutile) powders, *J. Chem. Phys.* **1969**, *50*, 1366–1370. https://doi.org/10.1063/1.1671199

X-ray Powder Data for Ore Minerals: The Peacock Atlas, Geological Society of America: Memoir 85, New York, **1962**.

(30) Berry, L. G. (Ed.). *Index (Inorganic) to the Powder Diffraction File*, American Society for Testing and Materials, Philadelphia, **1972**.

M
a
k
i
Infrared spectra for mineral identification, *Amer. Ind. Hyg. Ass. J.* **1970**, *31*, 100–108.

(32) Jovanovski, G.; Makreski, P.; Kaitner, B.; Šoptrajanov, B., Minerals from Macedonia. X-ray powder diffraction vs. vibrational spectroscopy in mineral identification, *Contributions Sec. Math. Tech. Sci. MANU* **2009**, *30*, 7–34. http://dx.doi.org/10.20903/csnmbs.masa.2009.30.1-2.22

P
Minerals from Macedonia. XXIII. Spectroscopic and structural characterization of schorl and beryl cyclosilicates, *Spectrochim. Acta Part A* **2009**, *73*, 460–467. https://doi.org/10.1016/j.saa.2008.07.011

(34) M
o
a
y
s
a
n
k
o
v
s
k
i
,
Channel occupancy in an alkali-poor beryl from Serra Branca (Goias, Brazil): spectroscopic characterization, *Am. Mineral.* **1996**, *81*, 395–403. https://doi.org/10.2138/am-1996-3-414

Theoretical and experimental study of the vibrational spectra of (para)symplesite and hornesite, *Spectrochim. Acta Part A* **2015**, *144*, 155–162. https://doi.org/10.1016/j.saa.2015.01.108

’Temperature-dependent vibrational dynamics of rutile (TiO_2) from molecular dynamics simulations and two-dimensional correlation analysis techniques, *Minerals* **2024**, *14*, Article 118. https://doi.org/10.3390/min14020118

K
i
.

(37) Moenke, M. *Mineralspektren*, Vol. II., Akademie-Verlag, Berlin, **1966**.

(38) R
o
j
o

(39) C
a
M
p
i
;Raman and infrared spectroscopic study of the vivianite-group phosphates vivianite, baricite and bobierrite, *Miner. Mag*. **2002**, *66*, 1063–1073. https://doi.org/10.1180/0026461026660077

(41) Chukanov, N. V.; Scholz, R.; Aksenov, S. M.; Rastsvetaeva, R. K.; Pekov, I. V.; Belakovskiy, D. I.; Krambrock, K.; Paniago, R.M.; Righi, A.; Martins, R. F.; Belotti, F. M.; Bermanec, V., Metavivianite, $Fe^{2+}Fe^{3+}_2(PO_4)_2(OH)_2{\cdot}6H_2O$: new data and formula revision, *Miner. Mag*. **2012**, *76*, 725–741. https://doi.org/10.1180/minmag.2012.076.3.20

(42) C
h
r
i
o
a
f
t
r
i
o
G
L
i

(43) f

(44) M
L
a
R
M
K
a
Raman and infrared spectroscopy of arsenates of the roselite and fairfieldite mineral subgroups, *Spectrochim. Part A*, **2009**, *71*, 1788–1794. https://doi.org/10.1016/j.saa.2008.06.039

(45) Frost, R. L.; Kloprogge, J. T.; Weier, M. L.; Martens, W.

(46) Hanafi, Z. M.; Alzewel, K. A.; Ibrahim, E. M. H.; Abou

(47) Kato, M.; Onari, S.; Arai, T. Far infrared and Raman spectra in $(As_2S_3)_{1-x}(Sb_2S_3)_x$ glasses, *Jpn J. Appl. Phys*. **1983**, *22*, 1382. https://doi.org/10.1143/JJAP.22.1382

The low-temperature Raman spectra of pyrargyrite (Ag_3SbS_3), *Solid State Commun*. **1983**, *45*, 227–230. https://doi.org/10.1016/0038-1098(83)90469-6

(49) Physico-chemical properties of $M_2^{VB}N_3^{VIB}$ compounds: Infrared absorption spectra measurement, *J. Phys. Chem*. **1975**, *94*, 291–295. https://doi.org/10.1524/zpch.1975.94.4-6.291

(50) Minceva-Šukarova, B.; Jovanovski, G.; Makreski, P.; Šoptrajanov, B.; Griffith, W. P.; Willis, R.; Grzetić, I. Vibrational spectra of $M^IM^{III}S_2$ synthetic minerals (M^I = Cu, Ag; M^{III} = As, Sb), *J. Mol. Struct.* **2003**, *651–653*, 181–189. https://doi.org/10.1016/S0022-2860(02)00105-4

A laser Raman microprobe study of some geologically important sulphide minerals, *Chem. Geol.* **1993**, *106*, 113–127.

Raman spectroscopy of selected arsenates — implications for soil remediation, *Spectrochim. Acta Part A* **2003**, *59*, 2241–2246. https://doi.org/10.1016/S1386-1425(03)00068-4

Spectroscopic and magnetic study of the $(Mg,M)_3(AsO_4)_2{\cdot}8H_2O$ ($M = Ni^{2+}$, Co^{2+}) arsenates, *Mater. Res. Bull*. **1996**, *31*, 925–934. https://doi.org/10.1016/S0025-5408(96)00088-8

https://doi.org/10.1016/0009-2541(93)90295-T

(52) K
h
a
r
b
i

(53) S
h
u
à
i

(54) K
à
d

X
i

Cyclic microwave assisted syntheses of Sb_2S_3 twin flowers in solutions containing a template and splitting agent, *Chalcogenide Lett*. **2012**, *9*, 365–370.

(56) Makreski, P.; Petruševski, G.; Ugarković, S.; Jo
Laser-induced transformation of stibnite (Sb_2S_3) and other structurally related salts, *Vib. Spectrosc*. **2013**, *68*, K
177–182. https://doi.org/10.1016/j.vibspec.2013.07.007

(57) A facile chemical conversion synthesis of Sb_2S_3 nanotubes and the visible light-driven photocatalytic activities, *Nanoscale Res. Lett.* **2012**, *7*, 199. https://doi.org/10.1186/1556-276X-7-199

Mineralspektren, Vol. I, Akademie-Verlag, Berlin, **1962**.

Vibrational spectra of the common silicates. 1. The garnets. *Am. Mineral*. **1971**, *56*, 54–71.

Vibrational spectroscopy of end-member silicate garnets, *Phys. Chem. Minerals* **1991**, *17*, 503–526. https://doi.org/10.1007/BF00202230

(61) G
a
r
n
i
f
S
i
Raman spectra of isolated and interconnected pyramidal SiS_4 groups (X = Sb, Bi) in stibnite, bismuthinite, orpiment, stephanite and bournonite, *Eur. J. Mineral.* **2009**, *21*, 325–332. https://doi.org/10.1127/0935-1221/2009/0021-0014

Raman scattering in silicate garnets: an investigation of their resonance intensities, *J. Raman Spectrosc.*, **1997**, *28*, 659–662. https://doi.org/10.1002/(SICI)1097-4555(199709)28:9<659::AID-JRS156>3.0.CO;2-7

(63) K
w

(64) C
Raman studies on rock-forming minerals. Part I. Orthosilicates and cyclosilicates, *J. Chem. Soc. A* **1969,** 1372–1377. https://doi.org/10.1039/J19690001372

(65) Makreski, P.; Jovanovski, G.; Runčevski, T.; Jaćimović, of rare earth elements in minerals by Raman spectroscopy instrumentation, *Maced. J. Chem. Chem. Eng*. **2011**, *30*, 241–250. https://doi.org/10.20450/mjcce.2011.39

The Raman spectroscopy of cement minerals under 1064 nm excitation, *Spectrochim. Acta Part A*, **1993**, *49*, 715–722. https://doi.org/10.1016/0584-8539(93)80094-Q

Raman or fluorescence spectra? About the use of FT-Raman techniques on inorganic compounds, *Appl. Spectrosc.* **1994**, *48*, 1028–1029. https://opg.optica.org/as/abstract.cfm?URI=as-48-8-1028

(68) A
n
a
m
a
c
a
i
2
i

Raman spectra of silicate garnets, *Phys. Chem. Minerals* **1998**, *25*, 142–151. https://doi.org/10.1007/s002690050097.

XRF and Raman characterization of antimonite, *In-*

calcium minerals, *Spectrochim. Acta Part A*, **1997**, *53*, 693–697. https://doi.org/10.1016/S1386-1425(96)01848-3

Necessary precautions in the Raman analysis of calcium phosphate minerals using 1.06 Mu M YAG laser excitation, *J. Anal. Chem*. **1998**, *52*, 1122–1126.

(70) A m i n z a d e

Laser induced fluorescence bands in the FT-Raman spectra of bioceramics, *Spectrochim. Acta Part A*, **2007**, *66*, 199–205.

(72) Lueth, V., Light sensitive minerals. In: *39th Annual New Mexico Mineral Symposium Abstracts,* Socorro, New Mexico, **2018**, pp. 34–35.

A Caring for geological collections: unresolved questions. *J. Nat. Sci. Collect.* **2021**, *8*, 28–38.

(74) G l i s h o s k a z a p , I . ; S i m o n s e n , R . ; W i l l i a m s , S .

Conserving light sensitive minerals and gems. In: *The Care and Conservation of Geological Materials: Minerals, Rocks, Meteorites and Lunar Finds*; Howie, F. M. (Ed.), Butterworth-Heinemann, Oxford, **1992**, pp. 11–24.

Natural fading of amethyst. *Gems Gemol*. **1985,** *21*, 115.

Amethyst, heat treated. *Gems Gemol*. **1985**, *21*, 43.

R., Colored varieties of the silica minerals. In: *Silica: Physical Behavior, Geochemistry, and Materials Applications*; Heaney, P.J.; Prewitt, C.T.; Gibbs, G.V. (Eds.), Mineralogical Society of America, **1994,** pp. 433–468.

The care of minerals, Section 3A: The curation of minerals. *J. Russel Soc.* **1985**, *1*, 94–114.

The care of minerals, Section 2: The development of museums. *J. Russel Soc.* **1983**, *1*, 54–77.

Pigments – arsenic based yellows and reds, *Archaeol. Anthropol. Sci.* **2022**, *14, 4.* https://doi.org/10.1007/s12520-021-01431-2

M. (Ed.), *The Care and Conservation of Geological Materials: Minerals, Rocks, Meteorites and Lunar Finds*, Butterworth-Heinemann, Oxford, **1992**, pp. 56–69.

Raman spectroscopic studies of CO_2 laser-irradiated human dental enamel, *Spectrochim. Acta Part A*, **1999**, *55*, 1303–1308. https://doi.org/10.1016/S1386-1425(99)00036-9

The light-induced alteration of realgar to pararealgar. *Am. Mineral.* **1992**, *77*, 1266–1274.

(83) Muniz-Miranda, M.; Sbrana, G.; Bonazzi P.; Menchetti, Spectroscopic investigation and normal mode analysis of As_4S_4 polymorphs. *Spectrochim. Acta Part A,* **1996**, *52*, 1391–1401. https://doi.org/10.1016/0584-8539(96)01698-4

(84) N a u m o v ,

(85) Naumov, P.; Makreski, P.; Petruševski, G.; Runčevski, Visualization of a discrete solid-state process with steady-state X-ray diffraction: observation of hopping of sulfur atoms in single crystals of realgar. *J. Am. Chem.Soc*. **2010**, *132*, 11398–11401. https://doi.org/10.1021/ja1030672

(86) Macchia, A.; Nunziante Cesaro, S.; Campanella, L.; M a k r e s k i ,

Which light for cultural heritage: Comparison of light sources with respect to realgar photodegradation. *J. Appl. Spectrosc*. **2013**, *80*, 637–643. https://doi.org/10.1007/s10812-013-9820-6

(87) P r a t e s i ,

Photoinduced effects of monochromatic visible light with different wavelengths on realgar, *J. Raman Spectrosc*. **2022**, *53*, 1533–1539. https://doi.org/10.1002/jrs.6408

The occurrence of monoclinic jarosite in natural environments, *Am. Mineral.* **2023**, *108*, 584–594. https://doi.org/10.2138/am-2022-8276

The jarosite process – past, present and future. In: *Lead*-J. (Eds), Metallurgical Society of AIME, Warrendale, **1980**, 97–123.

(91) S a n d ,

The role of iron-hydroxy precipitates in the passivation of chalcopyrite during bioleaching, *Miner. Eng.* **2000**, *13*, 1117–1127. https://doi.org/10.1016/S0892-6875(00)00095-9

(93) Spasovski, O.; Mirčovski, V., New data on the hydrothermal alterations in the Plavica deposit (eastern Macedonia), *Geologica Macedonica* **2008**, *22*, 9–16.

(94) Kerolli-Mustafa, M.; Bačić, I.; Ćurković, L., Investigation of jarosite process tailing waste by means of Raman and infrared spectroscopy, *Mat.-wiss. u. Werkstofftech* **2013**, *44*, 768–773. https://doi.org/10.1002/mawe.201300172

Magnetic behavior and infrared spectra of jarosite, basic iron sulfate, and their chromate analogs, *J. Solid State Chem.* **1975**, *13*, 1–13. https://doi.org/10.1016/0022-4596(75)90075-4

Infrared and Raman study of alunite-jarosite compounds, *Spectrochim. Acta Part A*, **1986**, *42*, 729–734. https://doi.org/10.1016/0584-8539(86)80092-7

Distinction of jarosite-group compounds by Raman spectroscopy, *Can. Mineral.* **1998**, *36*, 1225–1235.

Minerals from Macedonia. XIV. Identification of some sulfate minerals by vibrational (infrared and Raman) spectroscopy, *Vib. Spectrosc.* **2005**, *39,* 229–239. https://doi.org/10.1016/j.vibspec.2005.04.008

(99) B i s ,

(100) F r o s ,

XPS characterisation of chalcopyrite chemically and bio-leached at high and low redox potential, *Miner. Eng.* **2005**, *18*, 505–515. https://doi.org/10.1016/j.mineng.2004.08.004

(101) F r o ,

(102) L a n e , l .

Mid-infrared emission spectroscopy of sulfate and sulfate-bearing minerals, *Am. Mineral.* **2007**, *92*, 1–18. https://doi.org/10.2138/am.2007.2170

vvne visible and infrared spectral properties of jarosite and alunite, *Am. Mineral*. **2005**, *90*, 1100–1107. https://doi.org/10.2138/am.2005.1700

Raman and IR spectroscopic studies of alunite-supergroup compounds containing Al, Cr^{3+}, Fe^{3+} and V^{3+} at the B site, *Can. Mineral.* **2009**, *47*, 663–681. https://doi.org/10.3749/canmin.47.3.663

(104) S
p
r
a
l
l
,
The power of databases: the RRUFF project. In: *Highlights in Mineralogical Crystallography*, Armbruster, T.; Danisi, R.M. (Eds), De Gruyter, Berlin, **2015**, 1–30.

Infrared and Raman Spectra of Calculi, Elsevier, Paris, 1997.

Background removal from spectra by designing and minimising a non-quadratic cost function, *Chemometr. Intell. Lab. Syst*. **2005**, *76*, 121–133. https://doi.org/10.1016/j.chemolab.2004.10.003

Effect of hydrogen peroxide bleaching on bone mineral/matrix ratio, *Appl. Spectrosc*. **2002**, *56*, 1035–1037. https://doi.org/10.1366/000370202760249774

(109) G
l
c
L
k
,
Bone tissue fluorescence reduction for visible laser Raman spectroscopy, *Appl. Spectrosc*. **2002**, *56*, 182–186. https://doi.org/10.1366/0003702021954647

New preparation method of bone samples for Raman microspectrometry, *Appl. Spectrosc*. **1998**, *52*, 312–313. https://doi.org/10.1366/0003702981943428

(112) Kocademir, M.; Kumru, M.; Gölcük, K.; Suarez-
Fluorescence reduction in Raman spectroscopy by chemical bleaching on renal stones. *J. Appl. Spectrosc*. **2020**, *87*, 282–288. https://doi.org/10.1007/s10812-020-00997-1

(113) W
a
r
i
M
,
(114) M
E
s
e
C
i
a
e
(115) J
,
The crystal structure and vibrational spectroscopy of hydrosite and alunite minerals, *Am. Mineral.* **2013**, *98*, 1633–1643. https://doi.org/10.2138/am.2013.4486

(116) H
K
a
n
i
M
,
(117) D
R
a
f
i
M
,
(118) Stefov, V.; Šoptrajanov, B.; Spirovski F.; Kuzmanovski, I.; Lutz, H. Infrared and Raman spectra of magnesium ammonium phosphate hexahydrate (struvite) and its isomorphous analogues. I. Spectra of protiated and partially deuterated magnesium potassium phosphate hexahydrate, *J. Mol. Struct*. **2004**, *689*, 1–10. https://doi.org/10.1016/j.molstruc.2003.08.019

In vitro study of inhibitory effect of ficus benghalensis fruits extract on struvite crystals, *Int. J. Recent Sci. Res.* **2019**, *10*, 34932–34936. http://dx.doi.org/10.24327/ijrsr.2019.1009.4002

W.; Range, K.-J., The vibrational spectra of NH_4VO_3 at elevated temperatures and pressures, *Z. Naturforsch. B* **1987**, *42*, 843–852. https://doi.org/10.1515/znb-1987-0709

(119) Stefov, V.; Šoptrajanov, B.; Kuzmanovski, I.; Lutz, H. Infrared and Raman spectra of magnesium ammonium phosphate hexahydrate (struvite) and its isomorphous analogues. III. Spectra of protiated and partially deuterated magnesium ammonium phosphate hexahydrate, *J. Mol. Struct.* **2005**, *752*, 60–67. https://doi.org/10.1016/j.molstruc.2005.05.040

(120) F
r
o
s
t
,
Temperature-dependent μ-Raman investigation of struvite crystals, *Spectrochim. Acta Part A* **2016**, *158*, 18–23. https://doi.org/10.1016/j.saa.2016.01.005

(122) Makreski, P.; Todorov, J.; Makrievski, V.; Pejov, L.;
J
o
W
a
n
e
v
(123) F
s
k
o
L
s
t
,
(124) Mihailović, T.; Libowitzky, E.; Effenberger, H., Synthesis, crystal structure, infrared and Raman spectra of $BaFe^{3+}_3(AsO_4)_2(OH)_5$ — a Raman spectroscopic study of a hydroxy-arsenate mineral, *J. Raman Spectrosc.* **2011**, *42*, 56–61. https://doi.org/10.1002/jrs.2612

(125) F
r
o
s
t
,
Catalytic performance of the high and low temperature polymorphs of $(C_6N_2H_{16})_{0.5}[(VO)(HAsO_4)F]$: structural, thermal, spectroscopic and magnetic studies, *Dalton Transact*. **2010**, *39*, 834–846. https://doi.org/10.1039/B910553K

H.; Lezama, L.; Garitaonandia, J. S.; Arriortua, M. I.; Rojo, T., Hydrothermal synthesis, crystal structure, and spectroscopic and magnetic properties of a new organically templated mixed-anion fluoro-arsenate–phosphate iron(III) compound, $(C_6H_{14}N_2)[Fe_3(HAsO_4)_{1.33}(HPO_4)_{0.67}(AsO_4)_{0.84}(PO_4)_{0.16}F_4]$ ·0.5(H_2O), *Solid State Sci*. **2003**, *5*, 1291–1301. https://doi.org/10.1016/S1293-2558(03)00144-4

Raman spectroscopic study of the hydrogen-arsenate mineral pharmacolite $Ca(AsO_3OH)\cdot 2H_2O$—implications for aquifer and sediment remediation, *J. Raman Spectrosc*. **2010**, *41*, 1348–1352. https://doi.org/10.1002/jrs.2556

(129) Đorđević, T.; Karanović, L., Synthesis, crystal structure, infrared and Raman spectra of $Sr_4Cu_3(AsO_4)_2(AsO_3OH)_4\cdot 3H_2O$ and $Ba_2Cu_4(AsO_4)_2(AsO_3OH)_3$, *J. Solid State Chem*. **2008**, *181*, 2889–2898. https://doi.org/10.1016/j.jssc.2008.07.025

Raman spectroscopy of jesenkoite, lammerite and struvite, *Spectrochim. Acta Part A* **2005**, *62*, 181–188. https://doi.org/10.1016/j.saa.2004.12.024

(130) Đorđević, T.; Karanović, L., A new polymorph of $Ba(AsO_3OH)$: Synthesis, crystal structure and vibrational spectra, *J. Solid State Chem*. **2010**, *183*, 2835–2844. https://doi.org/10.1016/j.jssc.2010.09.027

Diguanidinium hydrogenarsenate monohydrate and its deuterated analogue: Vibrational, DSC and X-ray investigations, *Spectrochim. Acta Part A*, **2005**, *61*, 2809–2821. https://doi.org/10.1016/j.saa.2004.10.027

(131) Sejkora, J.; Čejka, J.; Frost, R. L.; Bahfenne, S.; Plášil, arsenate group (AsO_3OH) in solid-state compounds: copper mineral phase geminite $Cu(AsO_3OH)\cdot H_2O$ from different geological environments, *J. Raman Spectrosc.* **2010**, *41*, 1038–1043. https://doi.org/10.1002/jrs.2538

(132) F r o s t ,

(133) Čejka, J.; Sejkora, J.; Bahfenne, S.; Palmer, S. J.; Plášil, J.; Frost, R. L.; Čejka, J.; Sejkora, J.; Plasil, J.; Bahfenne, S.; Keeffe, E. C. Raman spectroscopy of hydrogene-arsenate group $(AsO_3OH)^{2-}$ in solid-state compounds: Cobalt mineral phase burgessite $Co_2(H_2O)_4[AsO_3OH]_2\cdot H_2O$, *J. Raman Spectrosc.* **2011**, *42*, 534–539. https://doi.org/10.1002/jrs.2675

(134) F e r r ,

(135) Y a r n i g s ; H ,

The crystal structure of pharmacolite, $CaH(AsO_4)\cdot 2H_2O$, *Acta Cryst. B*, **1969**, *25*, 1544–1550. https://doi.org/10.1107/S0567740869004304

E v a n s , H . ; D o w n s , T . ; J e n k i n s ,

The crystal structure of vladimirite, with a revised chemical formula, $Ca_4(AsO_4)_2(AsO_3OH)\cdot 4H_2O$, *Can. Mineral*. **2011**, *49*, 1055–1064. https://doi.org/10.3749/canmin.49.4.1055

(136) F r o s t ,

Symplesit felsőbányáról, *Természetrajzi Füzetek*, **1886**, *10*, 83–108.

Classification of *minerals* of the type $A_3(XO_4)_2\cdot nH_2O$ (concluded), *Am. Mineral*. **1940**, *25*, 787–809.

(139) i t K l o

The structure of vivianite and symplesite, *Acta Cryst.* **1950**, *3*, 1–6. https://doi.org/10.1107/S0365110X5000001X

Structure of vivianite and symplesite, *Nature* **1949**, *164*, 449–450. https://doi.org/10.1038/164449b0

(141) P e t g e S c h m e t z e r ,

(142) S c h ,

The symplesite problem, *Acta Cryst.* **1954**, *7*, 630. https://doi.org/10.1107/S0365110X54002137

Raman spectroscopy of some complex arsenate minerals – implications for soil remediation, *Spectrochim. Acta Part A*, **2003**, *59*, 2797–2804. https://doi.org/10.1016/S1386-1425(03)00103-3

, K . ; T r e m m e l , G . ; B a r t e l k e ,

Paragenese seltener minerale aus Bou-Azzer, Marokko: parasymplesit, symplesit, schneiderhöhnit, karibibit., *N. Jb. Mineral. Abh*. **1980**, *138*, 94–108.